AIAA
G-083-1999

Guide

Guide to Modeling Earth's Trapped Radiation Environment

AIAA
G-083-1999

Guide

Guide To Modeling Earth's Trapped Radiation Environment

Sponsor

American Institute of Aeronautics and Astronautics

Abstract

This Guide serves as both an introduction to the phenomena of radiation in the space environment and the product engineering issues facing spacecraft designers. Emphasis is on the trapped radiation environment of the Earth which is known as the Van Allen Belts. The leading empirical models are described and the problems in using them are identified. Current radiation modeling efforts are also discussed, along with shielding design and optimization. The Guide is intended for students, designers, mission planners, and others who need a ready understanding of this critical issue affecting spacecraft performance in Earth orbit.

Library of Congress Cataloging-in-Publication

AIAA guide to modeling earth's trapped radiation environment/sponsor,
American Institute of Aeronautics and Astronautics
p. cm.
"AIAA G-083-1999"
Includes bibliographical references
ISBN 1-56347-349-6 (softcover), 1-56347-367-4 (electronic)
1. Van Allen radiation belts—Mathematical models.
2. Magnetohydrodynamics—Mathematical models. I. American
Institute of Aeronautics and Astronautics.
QC809.V3G85 1999
538' .766—dc21 99-35575
CIP

Published by
American Institute of Astronautics and Aeronautics
1801 Alexander Bell Drive, Suite 500, Reston, VA 20191

Printed in the United States of America.

Contents

Foreword

With the increasing sophistication and high level of physical integration of electronics and electronic components, radiation effects have taken on a new significance in spacecraft design. The push toward "cheaper, better, faster" spacecraft has acerbated the trend toward increasingly more radiation sensitive parts. Indeed, trapped radiation effects on microelectronics have been and are continuing concerns for all spacecraft designers, builders, and users. The availability of new radiation data coupled with long term changes in the Earth's magnetic field and trapped radiation fluxes have generated the requirement for newer, more comprehensive tools for modeling the Earth's trapped radiation environment and its effects on space systems. Realizing this need, the AIAA Atmospheric and Space Environments Committee on Standards in February of 1997 commissioned the preparation of a reference guide that would describe the current status of radiation belt studies and review methods for attacking the issues associated with modeling the trapped radiation environment in a systematic, practical fashion. The intent was to point the way to increasingly better methods of testing, designing, and flying reliable spacecraft systems in the Earth's radiation environment. The guide was to serve as a review of the key concepts associated with modeling the radiation environment and its effects. It would describe the principle models of the trapped radiation environment currently available and recommend a long range plan for enhancing the capabilities in this important environmental area. The document presented here represents the primary product of the Committee's commission. As such, it is hoped that it will be widely disseminated and discussed in the space community with the intent of encouraging further debate on this complex technical issue. Ultimately, the end result should be more robust, survivable spacecraft systems capable of addressing the stringent needs of the 21st Century!

This Guide to Modeling Earth's Trapped Radiation Environment has been sponsored by the American Institute of Aeronautics and Astronautics (AIAA) as part of its Standards Program. The AIAA Standards Procedures provide that all approved Standards, Recommended Practices, and Guides are advisory only. Their use by an-one engaged in industry or trade is entirely voluntary. There is no agreement to adhere to any AIAA standards publication and no commitment to conform to or be guided by any standards report. In formulating, revising, and approving standards publications, the Committees on Standards will not consider patents which may apply to the subject matter. Prospective users of the publications are responsible for protecting themselves against liability for infringement of patents or copyrights, or both.

The guide was prepared by Dr. Henry B. Garrett of the Jet Propulsion Laboratory, the California Institute of Technology, Pasadena, CA for the AIAA Atmospheric and Space Environments Committee on Standards, Dr. Shu Lai, Chairman. This work was carried out at the Jet Propulsion Laboratory under a contract with NASA. Special thanks go to those who participated in the review of the document. In particular, Drs. Alfred Vampola and William Vaughan provided extremely useful and pertinent corrections.

The AIAA Atmospheric & Space Environments Committee on Standards approved the document in August 1999.

At the time of approval, the AIAA Atmospheric and Space Environment Committee on Standards included the following members:

Shu T. Lai (Air Force Research Laboratory), Chairman
Dana A. Brewer (NASA Headquarters)
Herbert C Carlson (Air Force Office of Scientific Research)
Phan D. Dao (Air Force Research Laboratory)
Adarsh Deepak (Science & Technology Corp.)
Gerald Dittberner (NOAA/NEDIS)
L. J. Ehernberger (NASA Ames-Dryden Facility)
Jeffrey M. Forbes (University of Colorado)

Henry B. Garrett (Jet Propulsion Lab.)
G. Barry Hillard (NASA Lewis Research Center)
Stuart L. Huston (Boeing Space & Defense)
JoAnn Joselyn (NOAA Space Environment Lab.)
Neil D. Kelley (National Renewable Energy Lab.)
O. Kenneth Moe (AF Space & Missile Systems Center)
Jerry Owens (NASA Marshall Space Flight Center)
Robert Sears (Jamieson Science & Engineering)
Robert A. Skrivanek (Visidyne Inc.)
Guy F. Spitale (Air Force Research Laboratory)
Walther Spjeldvik (Weber State University)
Robert M. Suggs (NASA Marshall Space Flight Center)
Gopal D. Tejwani (Lockheed Martin Space Operations)
Alfred Vampola (Consultant)
William W. Vaughan (UAH Research Center)
Robert E. Whitten (NASA Ames Research Center, retired)

The Standards Executive Council accepted the Guide for publication in August 1999.

1. Introduction

Increasing concerns over trapped radiation effects on microelectronics, coupled with the availability of new data, long-term changes in the Earth's magnetic field, and variations in the trapped radiation fluxes, have generated the need for better, more comprehensive tools for modeling the Earth's trapped radiation environment and its effects on space systems. The objectives of this guide are to describe the current status of those efforts and to review methods for attacking the issues associated with modeling the trapped radiation environment in a systematic, practical fashion. The ultimate goal will be to point the way to increasingly better methods of testing, designing, and flying reliable spacecraft systems in the Earth's radiation environment.

To set the stage for these discussions, a review of the key concepts associated with modeling the radiation environment and its effects will be presented first. The review will include a description of the principal models of the trapped radiation environment currently available. Recent results from radiation experiments on spacecraft such as CRRES, SAMPEX, and Clementine will then be described. The report will close with a detailed discussion of the current status of the modeling of the radiation environment and recommend a long-range plan for enhancing capabilities in this important environmental area.

Because of the increasing sophistication and high level of physical integration of electronics and electronic components, radiation effects have taken on a new significance in spacecraft design. For example, the rapid drop in power and voltage levels and the associated drop in feature size for integrated components (ICs) have greatly enhanced the ICs' sensitivities to single event effects (SEEs). The push toward commercial off-the-shelf parts has often led to parts that are much less radiation tolerant although this is not always true. Overall, the requirements for "cheaper, better, faster" spacecraft have acerbated this trend toward parts that are increasingly more radiation sensitive. The result is that, far from going away with time, radiation effects—both total ionizing dose and single event effects—are increasingly coming to dominate the design concerns for satellite manufacturers across the board. Add to this the desire of many new multisatellite communications providers to place their constellations in the middle of the harshest part of the radiation belts, and accurate modeling of the trapped radiation environment and its effects becomes a very real, long-term problem for the spacecraft community in general.

Solving the problems of trapped radiation effects on spacecraft is not as simple as just developing better models or more shielding. Although these are solutions in many situations, in general, most commercial spacecraft designers cannot afford either the large uncertainties in the current models or the extra mass necessary to cover the required design margins. Rather, proper design of radiation resistant systems requires complex trade-offs among parts, shielding, software, operations, redundancy, and orbit configuration. Each of these "solutions" is subject to uncertainty and has a cost impact on the final design. Unfortunately, the key component, the trapped radiation environment itself, is not well defined (observations and predictions that vary by factors of two for 5–11 year missions in Earth orbit are considered to be in excellent agreement; for shorter missions, factors approaching 10–100 are easily possible). Even given an accurate "average" description of the environment, short-term variations of several orders of magnitude in dosage and single event upset (SEU) rates have been seen in the span of hours (e.g., the 1989 solar proton events). Complicating the practical application of the radiation environment to spacecraft design, radiation transport codes and estimates of the effects of radiation damage are often inaccurate. Comparisons between ground tests and in situ measurements have shown significant disagreement. Furthermore, the parts used on the spacecraft can show variations in sensitivity of factors of 2–10, even within the same parts lot. Often, how a system is actually used can mask, or hopefully limit, the effects of radiation damage.

Thus, to a degree, mitigating radiation effects is a black art and, increasingly, a very expensive art for which any imprecision in the knowledge of the trapped radiation environment becomes a critical component. However, the ultimate solution is a comprehensive process that treats all uncertainties.

2. The Space Radiation Environment: Basic Concepts

This section provides an overview of the basic physical concepts and definitions that will be used throughout the guide. In particular, the concepts of energy, flux, fluence, and dosage will be briefly described. The reader is referred to the many excellent texts on space physics or astronomy for more detailed explanations.[1,2]

First consider the concept of energy. In the case of particles that have a rest mass, the fundamental equation relating particle mass and velocity to kinetic energy is:

$$E = (\gamma - 1) m_0 c^2 \qquad \text{Relativistically} \qquad (1)$$

$$= \frac{1}{2} m_0 V^2 \qquad \text{Non-Relativistically}$$

where

m_0 = particle rest mass
V = particle velocity
c = speed of light
E = particle kinetic energy
$\gamma = \left(1 - \frac{V^2}{c^2}\right)^{-1/2}$

For photons (which have no rest mass), the equivalent equation is:

$$E = h\nu \qquad (2)$$

where

h = Planck's constant
ν = frequency of the light

Closely coupled to the concept of energy is that of dose. Simply put, dose is the total energy accumulated in a given volume element of a specific material due to incident radiation. It is typically given in units of rads or "radiation absorbed dose" for a particular material (the material *must* be specified because energy absorption is dependent on the material). As an example, for silicon, 1 rad (Si) = 10^{-2} J/kg (Si). It must be emphasized that, for the same incident flux, different materials will be affected differently depending on the composition of the radiation and the composition of the absorbing material.

In addition to the energy and composition of a particle or photon, it is also necessary to describe how many of them there are. This is usually done in terms of intensity or flux and, when speaking in terms of a time interval, fluence. Confusion arises over the concepts of intensity/flux and fluence because there are many different ways to define these quantities. Here, we will define the quantity "unidirectional differential intensity" $j(E,\theta,\phi,t)$ as:

> The flux (number of particles or photons per unit time) of a given energy E per unit energy interval dE in a unit solid angle ($d\Omega = 2\pi \cos\theta \, d\theta \, d\phi$) about the direction of observation (in the θ,ϕ direction), incident on unit of surface area (dA) perpendicular to the direction of observation.

This is illustrated in Fig. 1.[2] Typical units are particles·$\mathrm{cm}^{-2}\cdot\mathrm{s}^{-1}\cdot\mathrm{sr}^{-1}\cdot\mathrm{keV}^{-1}$ for protons or electrons and particles·$\mathrm{m}^{-2}\cdot\mathrm{s}^{-1}\cdot\mathrm{sr}^{-1}\cdot(\mathrm{MeV}\cdot\mu^{-1})^{-1}$ for heavy ions (where μ is nucleon). A typical spectrum for iron cosmic rays is presented in Fig. 2.[3] In the figure, the solid curves are for solar maximum (lower) and solar minimum (upper). The dashed curve is the 90% worst case iron spectrum, which is implied by comparison with the cosmic ray helium spectrum. The “unidirectional integral intensity” (or flux) is defined as the intensity of all particles with energy greater than or equal to a threshold energy *E*:

$$j_{\geq E} = \int_E^\infty j \mathrm{d}E \tag{3}$$

with units of particles $\mathrm{cm}^{-2}\mathrm{s}^{-1}\mathrm{sr}^{-1}$.

We define the “omnidirectional flux” *J* as:

$$J = \int_{4\pi} j \mathrm{d}\Omega \tag{4}$$

Fluence *I* is the integral of the flux over a given time interval (e.g., one hour, one year):

$$I = \int_{\delta t} j \mathrm{d}t \tag{5}$$

Here, when we refer to omnidirectional fluence $I(\geq E)$, we will normally mean the “omnidirectional integral (in energy) fluence” such that:

$$I_{\geq E} = \int_{\mathrm{E}}^\infty \mathrm{d}E \int_{4\pi} \mathrm{d}\Omega \int_{\delta t} j \mathrm{d}t \tag{6}$$

The units of this quantity are particles·cm^{-2} for some specified threshold energy *E* (typically 1 MeV or higher for radiation effects) and for a specified time interval (often one year).

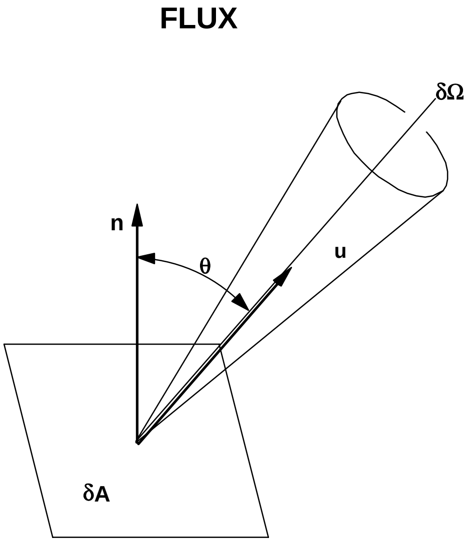

Figure 1 — The flux of a given energy *E* per unit energy interval *dE* in a unit solid angle about the direction of observation (Copyright by and used by permission of Springer-Verlag, New York)

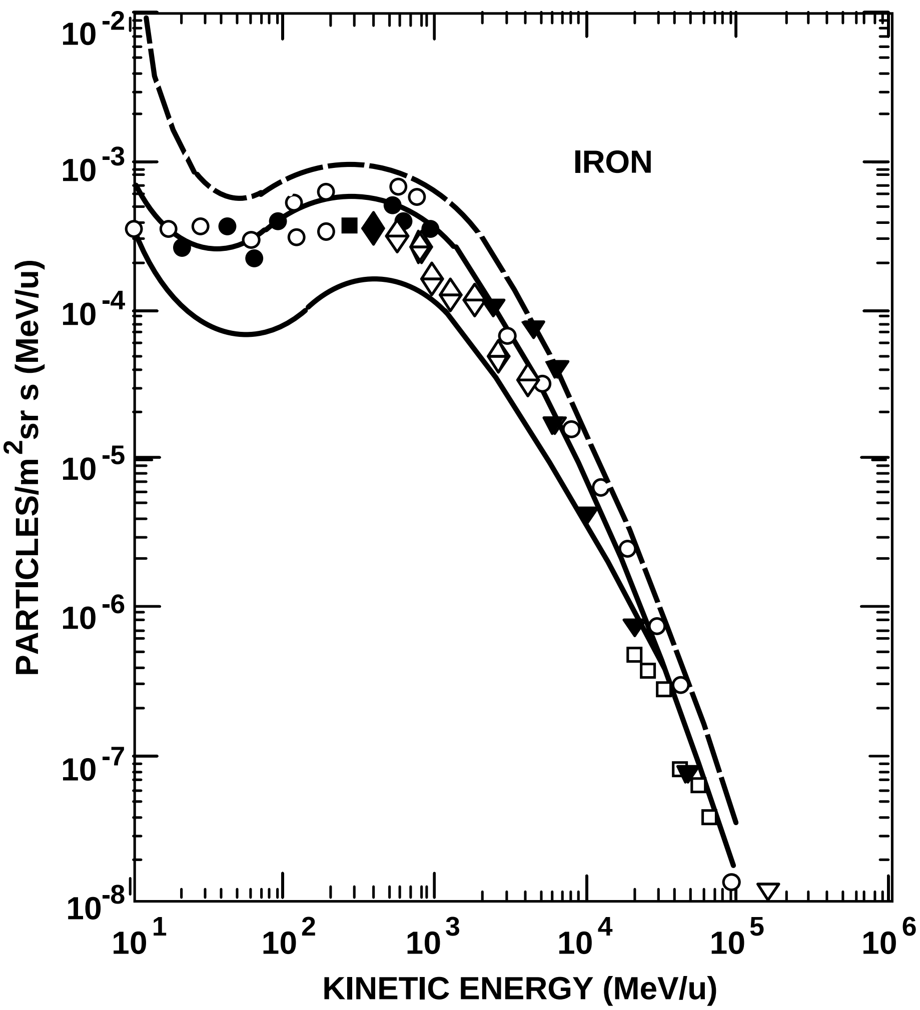

Figure 2 — The iron cosmic ray spectrum

To allow comparisons among different energies, particle types, and dosages, it is common practice to talk in terms of “1-MeV equivalent” (typically 1-MeV electrons or 1-MeV neutrons in silicon). First, the energy dependence of the damage and energy content of the spectra for the environment to be considered are used to determine what fluence of 1-MeV particles (electrons or neutrons) would produce the same amount of damage or dose in the material (typically silicon or aluminum). A curve for neutrons, in units of MeV-mb (where b is a barn or 10^{-24} cm^2 and the relative displacement damage is defined in terms of the cross section times the energy of the incident particle), is given in Fig. 3.[4] As an illustration, for 14 MeV neutrons, the 1-MeV neutron dose damage equivalent is given by multiplying the 14 MeV dose by 2.5 (obtained from Ref. 4). (Note: because of variations in the damage parameter with material and property, it should always be kept in mind that the use of a damage equivalent is not exact but an approximation for comparison purposes.)

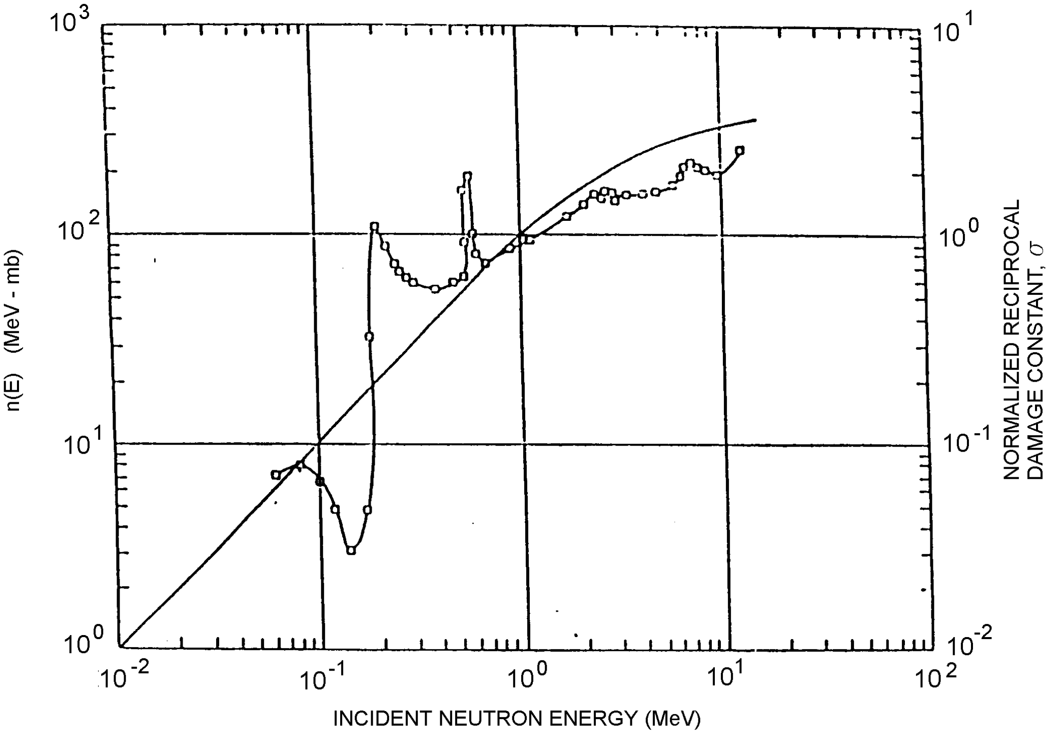

Figure 3 — Neutron displacement damage equivalence curve (Copyright by and used by permission of Institute of Electrical and Electronics Engineers)

A final quantity related to energy absorption and flux is the Linear Energy Transfer (LET). The LET is the energy transferred by radiation per unit length of absorbing material. That is, LET is proportional to d*E*/d*x* (note: there is in fact a slight difference between "energy transferred" and "energy lost per unit length" but that will be ignored here). For ionization and excitation effects, LET is often expressed in MeV/μm of the primary particle track length or, if the density of the material is known, MeV·cm^2·mg^{-1} (this is typically the unit when the reference is to an LET between 1 and 30 and is given by: $\frac{1}{\rho}\frac{dE}{dx}$).

The concept of LET is particularly important when discussing single event upsets (SEUs) or "soft errors." These occur when a particle, typically an ionized, high energy atomic nucleus, deposits enough energy in the sensitive region of an electronic device to cause a change in the logic state of the device. Upsets occur only when the energy deposited exceeds a critical level in the sensitive region of the device. This is often computed in terms of LET. When viewed as a function of LET, the probability of upset is, in its simplest form, a threshold phenomenon: any particle with a minimum LET of L_0 or greater will cause an upset. This behavior is illustrated in Fig. 4 where the energy deposited per unit length (LET) is plotted vs incident particle energy—note how the curve has a peak rate. L_0 corresponds to a constant value of LET. As illustrated, there can be multiple values of energy (E_1 and E_2 here) that correspond to the same value of LET. A useful way of presenting the environment in terms of LET is the Heinrich curve. The Heinrich curve gives the integral flux as a function of LET rather than particle energy. The Heinrich flux F_H is the flux of particles for a single species with a (threshold) LET of LET_0 or greater:

$$F_H(LET_0) = \int_{E_1}^{E_2} f_i(E)\,dE \qquad (7)$$

where f_i is the particle flux for the species i as a function of energy and E_1 and E_2 are the energies between which the LET is greater than or equal to the threshold LET_0 (a representative integral Heinrich curve for iron is plotted in Fig. 5[5]). The LET depends not only on particle energy, but on the target material as well because the LET vs energy curve will be different for all particle species. Experiments have shown, however, that to the first order it is the LET that is important for determining upsets and not the particle energy or its species. The Heinrich flux vs LET plot is the principal means of presenting radiation data for use in SEU calculations just as the particle flux vs energy is the main means of presenting radiation data for use in dosage calculations.

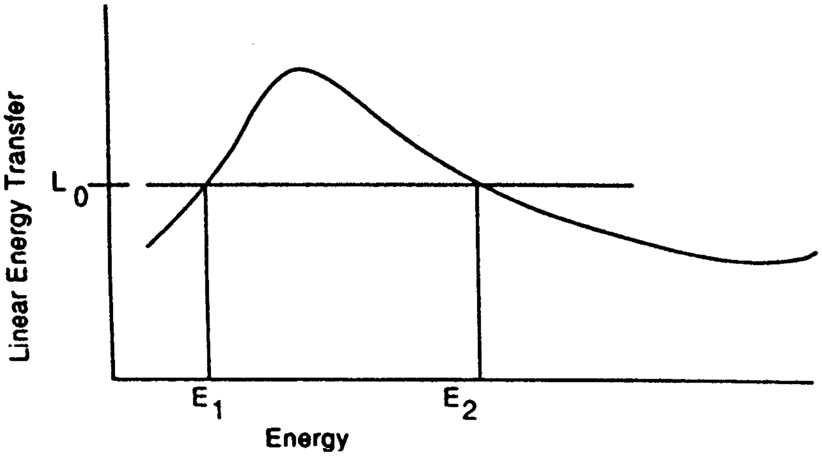

Figure 4 — Linear Energy Transfer Function (LET) vs Energy

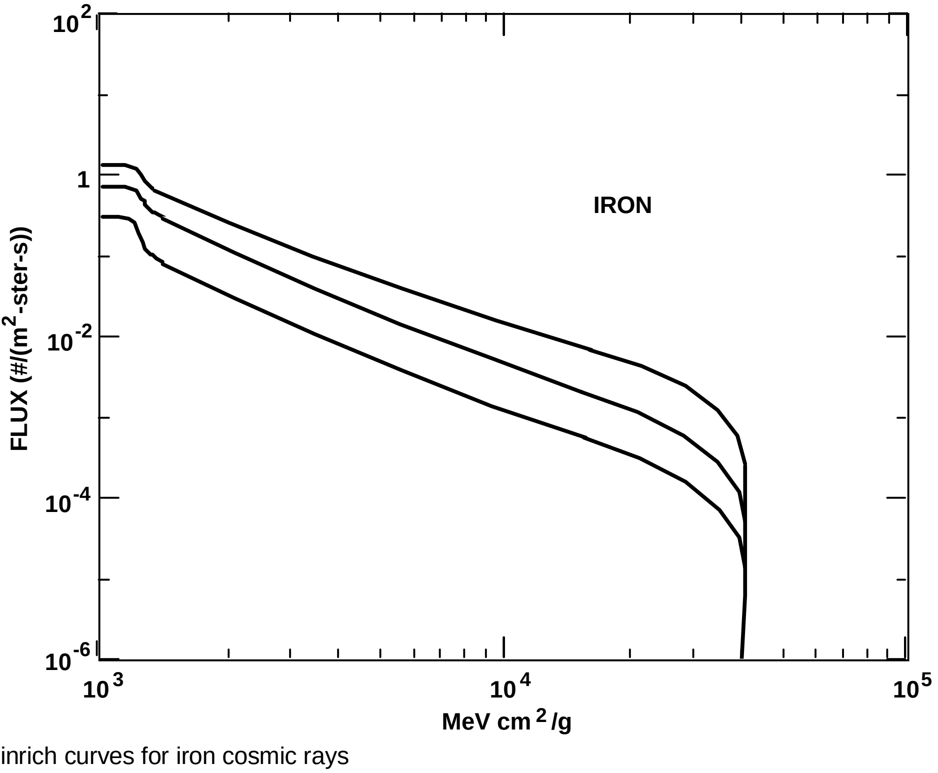

Figure 5 — Heinrich curves for iron cosmic rays

To summarize, this section has defined the basic terminology used to describe the radiation environment—dose, flux/intensity, fluence, LET, and 1-MeV equivalent. The reader is referred to books and articles by Roederer[2] and others for more complete descriptions of these concepts.

3. The Trapped Radiation Environment

3.1 Overview

By definition, the high energy particle radiation environment in space consists of electrons with energies greater than 40 KeV, protons or neutrons with energies greater than 1 MeV, and heavy ions with energies above 1 MeV/nucleon. Lower energy electrons, protons, and ions are ubiquitous but are considered as plasma. The populations are characterized in terms of their kinetic energy, charge state (or lack thereof), and composition. Unlike photons, which travel uniformly at the speed of light, particles can vary in velocity from a few m/s to a sizable fraction of the speed of light as in the case of cosmic rays. The high energy radiation population can be roughly divided into four families based on these characteristics:

1) Galactic cosmic rays, which consist of interplanetary protons, electrons, and ionized heavy nuclei.
2) Trapped radiation (for the Earth, the Van Allen belts).
3) Protons and heavy nuclei associated with solar proton events.
4) Neutrons (primarily cosmic ray albedo neutrons [CRAN] particles).

The first population changes relatively slowly (cyclically with the solar cycle). It is included here because it is believed to contribute to the CRAN and the trapped heavy ion population (see Section 6.2). The second population, the Earth's trapped radiation environment, can be divided into zones. Typically, the inner zone is populated with very high energy protons produced by CRAN decay and lower energy electrons, which also vary on a solar cycle timescale. The outer zone consists primarily of more energetic electrons and lower energy protons, which vary rapidly on a timescale that can be as short as one day, or less, in response to magnetic storms. The third population is highly time dependent, being associated with infrequent coronal mass ejections (CMEs). The fourth is a secondary population because the relatively short lifetime of neutrons severely limits any solar-produced fluxes at 1 AU or beyond. Each type of radiation has a characteristic spectrum and preferred interaction mode with matter that supports this simple division. Here, the discussion will focus primarily on the trapped radiation environment, the Van Allen belts.

First discovered by James Van Allen and his collaborators on Explorer I, trapped radiation at the Earth consists principally of energetic protons and electrons, with lesser percentages of heavy ions such as O^+, contained by the Earth's magnetic field in toroidal belts. Commonly known as the "Van Allen belts,"[6] these toroidal regions consist of (at least) two zones or belts. The inner belt extends from approximately hundreds of kilometers to ~6000 km in altitude and is populated by high energy (approximately tens of mega electronvolts) protons and medium energy (50–1000 keV) electrons, while the outer belt, up to 60,000 km in altitude, is predominately populated by high energy electrons. Schematics of the radiation flux contours for the Van Allen belts are illustrated in Fig. 6 where the average omnidirectional integral fluxes above energy thresholds are shown for 1-MeV electrons and 10-MeV protons.[7] The detailed mechanism by which particles are entrapped in the belt regions is not well understood nor is the primary source clearly identified (albedo neutrons are considered an important source of the intense proton and electron fluxes in the inner belt, while the outer belt may be primarily due to the geomagnetic field entrapping low energy solar wind plasma followed by local acceleration) although observations of abundance ratios imply both terrestrial and interplanetary sources.

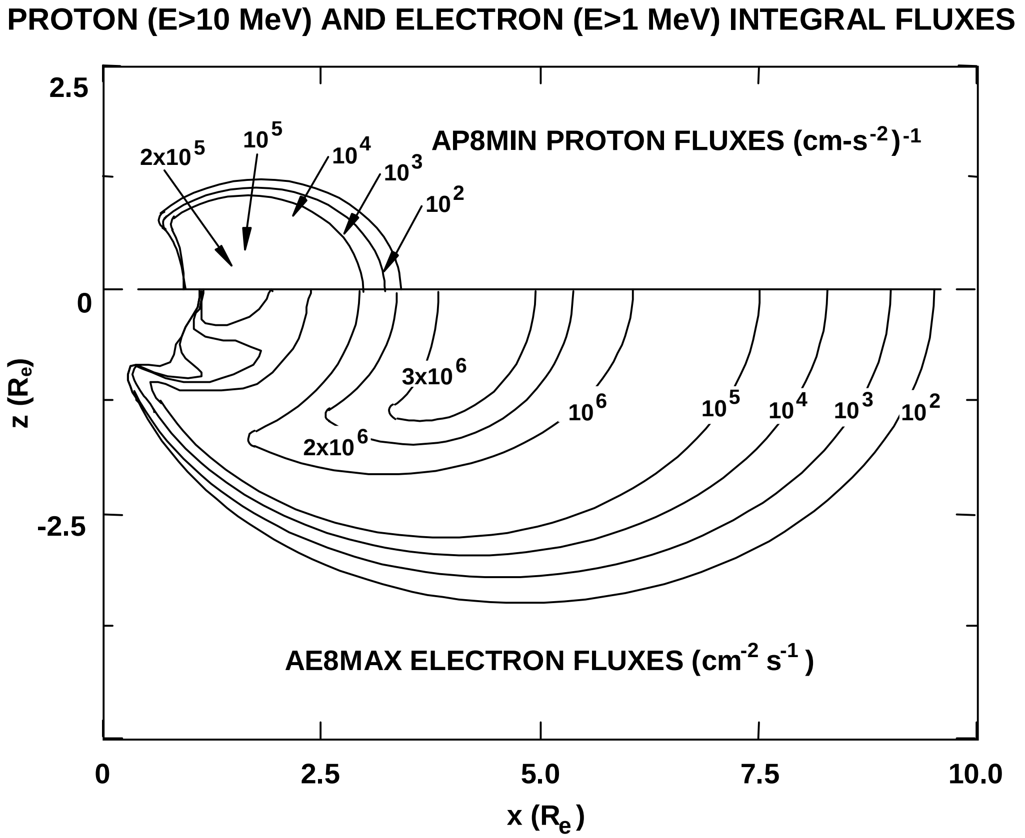

Figure 6 — The Earth's radiation belts in idealized space, according to the AP8 and AE8 models

Once captured, the motion of charged particles in the Earth's magnetic field is governed by the Lorentz force. The trapped radiation environment also exhibits large temporal variations. The inner belt zone, because of the dominance of the Earth's main field, is relatively stable. Most temporal variations in this population occur as the solar cycle proceeds and the Earth's neutral atmospheric density at a given altitude changes, causing variations in the altitude at which radiation particles can mirror without being scattered. Variations of an order of magnitude over a period of months have been observed in the electron flux intensities[8] as a result of extended elevated geomagnetic activity. In contrast, the outer belt, which is more influenced by the Earth's highly variable geomagnetic tail, experiences greater and more rapid (less than one day) temporal fluctuations. The electron concentration in the outer zone may experience temporal fluctuations as large as a factor of 100,000.

To better understand the preceding description, we first discuss the primary characteristics of the Earth's magnetic field because it is the dominate force controlling the formation of and changes associated with the trapped radiation belts. Following this discussion, a brief review of the basic concepts of particle entrapment such as gyro radius, mirror point, and pitch angle will be presented. Although the details of these concepts are not critical to understanding the basic effects of radiation on spacecraft, they are critical to understanding how the radiation belts are modeled and how the external dose on a particular vehicle is determined. In particular, the concept of adiabatic invariants will be summarized; this concept is critical to understanding why we use *B–L* coordinates, the basis of almost all modern radiation models, in describing the radiation belts. Following these descriptions, several examples of the trapped radiation environment will be presented in terms of the AE8/AP8 radiation models and the predictions compared with actual data. As will become evident, given the rapid temporal variations observed in the space environment, models are only reliable in a long-term predictive sense—which is a crucial issue in establishing design margins for spacecraft.

3.2 Geomagnetic Field

Above 1000 km, the dominant geophysical environment of interest is the magnetic field of the Earth—the source of the Earth's magnetosphere. Below 1000 km, the Earth's magnetic field, primarily through the control of the ionospheric plasma, plays an important though reduced role in the dynamics of the natural environment. The Earth's geomagnetic field B is composed of three distinct components (or current systems): the core field, crustal field, and external field.[9] The core field is a steady field due primarily to the convective motion of the conducting fluid in the Earth's internal core. The distribution of the crustal field, which is the remnant or induced magnetization of ferromagnetic materials near the Earth's surface, results in surface magnetic anomalies associated with the geologic and tectonic features of the crust. The core and crustal fields are usually combined and referred to as the internal or main field B_i. B_i varies slowly on the order of 100 years—currently ~0.05% per year—as illustrated in Fig. 7[9] (be aware that although it is critical to use a magnetic field model appropriate for the year in which the magnetic field estimates are required, it is typical in radiation modeling to use the magnetic field model for the year in which the radiation belt model was derived; this has caused serious problems in the past). B_i dominates at low Earth orbit (LEO) and accounts for more than ~99% of B, even during extremely large geomagnetic storms (massive variations in the Earth's magnetosphere brought about by changes in the solar environment that encompasses the Earth's magnetic field). In contrast, the external field B_e, which makes up ~1% of the field at LEO, is due primarily to extraterrestrial sources—the Earth's ring current and the solar wind. It varies rapidly in time (from on the order of milliseconds to periods as long as the 11-year solar cycle) and is closely correlated with geomagnetic activity and solar interactions. Models of the external component of the geomagnetic field are available but are of limited importance to the trapped radiation belts.[10–12]

Seven basic quantities, called magnetic elements, are used to specify the geomagnetic field.[9] Their definitions and relations are given in Fig. 8. Three independent quantities [e.g., (H, D, Z) or (X, Y, Z)] are required to uniquely define B. For spacecraft operating in the radiation belts, the most convenient system to use is either the geographic (also known as geocentric) or the geomagnetic coordinate system. These systems, based on spherical coordinates, are schematically defined in Fig. 9. Geographic coordinates correspond to a geocentric longitude/latitude system based on the Greenwich Prime Meridian. Geomagnetic coordinates are similarly Earth centered but have the north pole of the system passing near the geomagnetic pole, which is offset from the geographic pole, at ~78.5° latitude and ~291.1°E. Geomagnetic longitude is measured from the great circle passing through the geographic and geomagnetic poles. Details about other coordinate systems can be found in Knecht and Shuman.[9]

Aside from the gravitational field of the Earth, the magnetic field due to the internal geomagnetic field is the most accurately known of the natural environments. It can be crudely modeled in terms of a tilted (–11 deg from geographic north) magnetic dipole of magnitude $M = 8 \times 10^{25}$ G·cm^3 (G is the magnetic unit Gauss). Momentarily ignoring the tilt in the geomagnetic coordinate system, the magnetic field intensity induced by M at the point (r,θ,ϕ) is given by the expression:

$$B_i = -\left(M/r^3\right)\left(3\cos\theta + 1\right)^{1/2} \tag{8}$$

In the Gaussian unit system, r is in cm and B_i is in G. Given the above value for M, B_i is then found to have a maximum value of ~0.6 G near the polar cap and a minimum value of ~0.3 G near the equator at the Earth's surface.

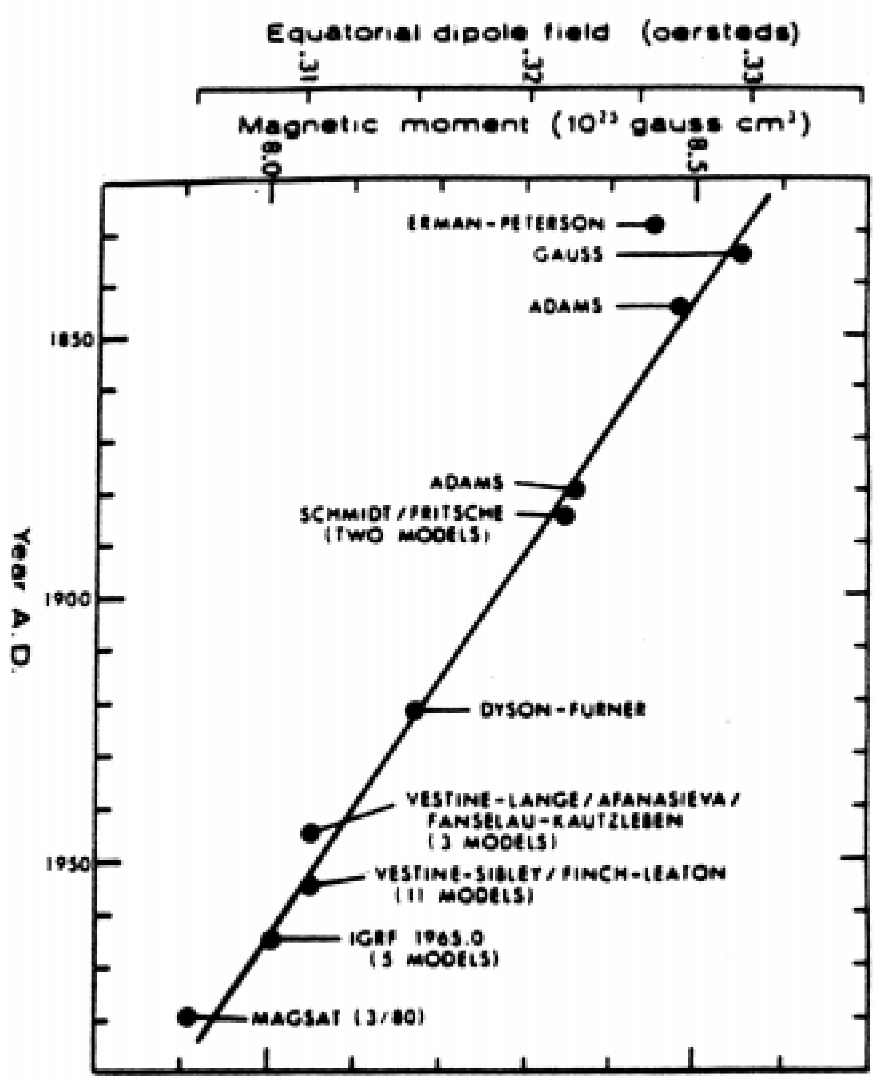

Figure 7 — Decay of the equatorial dipole field strength with time

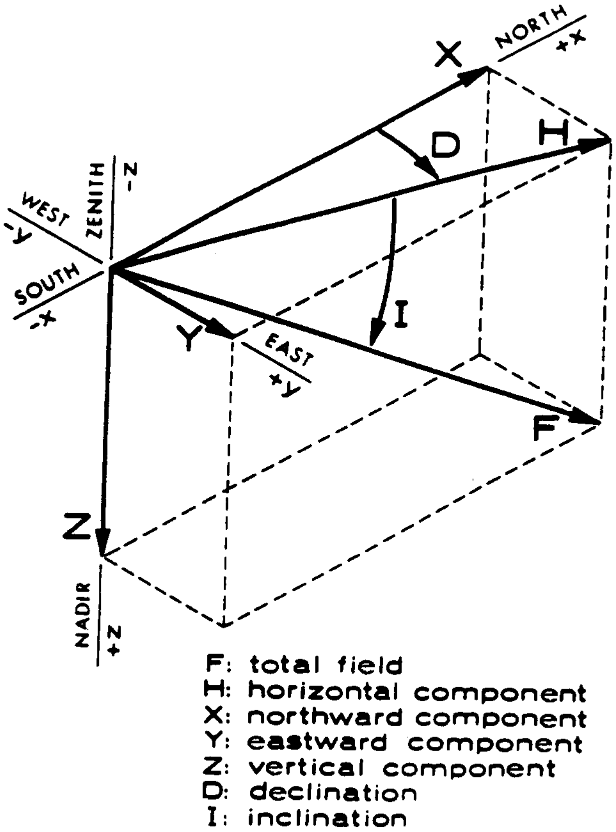

Figure 8 — Geomagnetic field magnetic elements

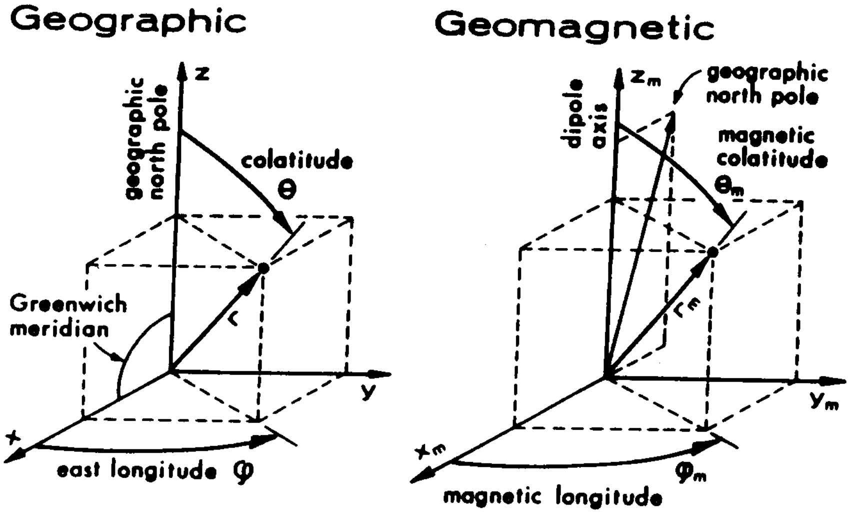

Figure 9 — Spherical coordinate system for geographic and geomagnetic coordinates

Equation (8) is valid only for an idealized configuration of a centered dipole. In reality, large scale discrepancies (as high as ±25%) exist between the measured data and the ideal, dipole expression. Modifying the configuration from a centered dipole to an eccentric dipole reduces the discrepancies to the ~10% level, but this is still unacceptably large. For most purposes, the International Geomagnetic Reference Field (IGRF) series of models is the official standard. The latest version, IGRF-95,[13] is a computer model based on the numerical fitting of measured data with a magnetic scalar potential expanded in terms of spherical harmonics.[13,14] The model calculates the seven magnetic elements of B_i for any given geographical location. Specifically, a scalar potential is found such that:

$$V(r,\theta,\phi) = a\sum_{n=1}^{N}\ \sum_{m=0}^{n}\Big\{\big[g_{n,m}\cos m\phi + h_{n,m}\sin m\phi\big]\left(a/r\right)^{n+1} + \big[A_{n,m}\cos m\phi + B_{n,m}\sin m\phi\big]\left(r/a\right)^{n}\Big\}P_{n,m}(\cos\theta) \tag{9}$$

where

a = radius of the Earth
r = radial distance in units of a
N = order of expansion
θ = colatitude
ϕ = east longitude
$g_{n,m}$, $h_{n,m}$ = constants for internal terms
$A_{n,m}$, $B_{n,m}$ = constants for external terms

The magnetic field components are then given by:

$$\begin{aligned} B_r &= -\frac{\partial V}{\partial r} \\ B_\theta &= -\frac{1}{r}\frac{\partial V}{\partial \theta} \\ B_\phi &= -\frac{1}{r\sin\theta}\frac{\partial V}{\partial \phi} \end{aligned} \tag{10}$$

Values of g and h are presented in Table 1 for the IGRF internal model. As discussed earlier, the epoch of the magnetic model is important and should correspond either to the same date as the date of the radiation model used or to a model epoch as close to the present as possible if only the current magnetic field value is desired.

TABLE 1. Spherical-Harmonic Coefficients for the IGRF/DGRF.[13]

	n	g/h m	DGRF 1985	DGRF 1990	IGRF 1995	dB/dt nT/yr*
g	1	0	–29873	–29775	–29682	17.6
g	1	1	–1905	–1848	–1789	13
h	1	1	5500	5406	5318	–18.3
g	2	0	–2072	–2131	–2197	–13.2
g	2	1	3044	3059	3074	3.7
h	2	1	–2197	–2279	–2356	–15
g	2	2	1687	1686	1685	–0.8
h	2	2	–306	–373	–425	–8.8
g	3	0	1296	1314	1329	1.5
g	3	1	–2208	–2239	–2268	–6.4
h	3	1	–310	–284	–263	4.1
g	3	2	1247	1248	1249	–0.2
h	3	2	284	293	302	2.2
g	3	3	829	802	769	–8.1
h	3	3	–297	–352	–406	–12.1
g	4	0	936	939	941	0.8
g	4	1	780	780	782	0.9
h	4	1	232	247	262	1.8
g	4	2	361	325	291	–6.9
h	4	2	–249	–240	–232	1.2
g	4	3	–424	–423	–421	0.5
h	4	3	69	84	98	2.7
g	4	4	170	141	116	–4.6
h	4	4	–297	–299	–301	–1
g	5	0	–214	–214	–210	0.8
g	5	1	355	353	352	0.1
h	5	1	47	46	44	0.2
g	5	2	253	245	237	–1.5
h	5	2	150	154	157	1.2
g	5	3	–93	–109	–122	–2
h	5	3	–154	–153	–152	0.3
g	5	4	–164	–165	–167	–0.1
h	5	4	–75	–69	–64	1.8
g	5	5	–46	–36	–26	2.3
h	5	5	95	97	99	0.9
g	6	0	53	61	66	0.5
g	6	1	65	65	64	–0.4
h	6	1	–16	–16	–16	0.3
g	6	2	51	59	65	0.6
h	6	2	88	82	77	–1.6
g	6	3	–185	–178	–172	1.9
h	6	3	69	69	67	–0.2
g	6	4	4	3	2	–0.2
h	6	4	–48	–52	–57	–0.9
g	6	5	16	18	17	–0.2
h	6	5	–1	1	4	1
g	6	6	–102	–96	–94	0
h	6	6	21	24	28	2.2
g	7	0	74	77	78	–0.2
g	7	1	–62	–64	–67	–0.8
h	7	1	–83	–80	–77	0.8
g	7	2	3	2	1	–0.6
h	7	2	–27	–26	–25	0.2
g	7	3	24	26	29	0.6
h	7	3	–2	0	3	0.6
g	7	4	–6	–1	4	1.2
h	7	4	20	21	22	–0.4
g	7	5	4	5	8	0.1
h	7	5	17	17	16	0
g	7	6	10	9	10	0.2
h	7	6	–23	–23	–23	–0.3
g	7	7	0	0	–2	–0.6
h	7	7	–7	–4	–3	0
g	8	0	21	23	24	0.3
g	8	1	6	5	4	–0.2
h	8	1	12	10	12	0.4
g	8	2	0	–1	–1	0.1
h	8	2	–19	–19	–20	–0.2
g	8	3	–11	–10	–9	0.4
h	8	3	5	6	7	0.2
g	8	4	–9	–12	–14	–1.1
h	8	4	–23	–22	–21	0.7
g	8	5	4	3	4	0.3
h	8	5	11	12	12	0
g	8	6	4	4	5	0.2
h	8	6	14	12	10	–1.2
g	8	7	4	2	0	–0.9
h	8	7	–15	–16	–17	–0.7
g	8	8	–4	–6	–7	–0.3
h	8	8	–11	–10	–10	–0.6
g	9	0	5	4	4	0
g	9	1	10	9	9	0
h	9	1	–21	–20	–19	0
g	9	2	1	1	1	0
h	9	2	15	15	15	0
g	9	3	–12	–12	–12	0
h	9	3	9	11	11	0
g	9	4	9	9	9	0
h	9	4	–6	–7	–7	0
g	9	5	–3	–4	–4	0
h	9	5	–6	–7	–7	0
g	9	6	–1	–2	–2	0
h	9	6	9	9	9	0
g	9	7	7	7	7	0
h	9	7	9	8	7	0
g	9	8	1	1	0	0
h	9	8	–7	–7	–8	0
g	9	9	–5	–6	–6	0
h	9	9	2	2	1	0
g	10	0	–4	–3	–3	0
g	10	1	–4	–4	–4	0
h	10	1	1	2	2	0
g	10	2	3	2	2	0
h	10	2	0	1	1	0
g	10	3	–5	–5	–5	0
h	10	3	3	3	3	0
g	10	4	–2	–2	–2	0
h	10	4	6	6	6	0
g	10	5	5	4	4	0
h	10	5	–4	–4	–4	0
g	10	6	3	3	3	0
h	10	6	0	0	0	0
g	10	7	1	1	1	0
h	10	7	–1	–2	–2	0
g	10	8	2	3	3	0
h	10	8	4	3	3	0
g	10	9	3	3	3	0
h	10	9	0	–1	–1	0
g	10	10	0	0	0	0
h	10	10	–6	–6	–6	0

Figures 10a and 10b show the three-dimensional character of the Earth's magnetic field. Figure 10a is a cross section of the Earth's magnetic field in the noon–midnight meridian showing the structure of the field lines and the plasma regions they contain. Figure 10b illustrates typical results from calculations of the magnetic field amplitude over the northern hemisphere at a constant altitude of 400 km. The field amplitude varies from a minimum of 0.25 G near the equator to 0.5 G over the polar caps. Two peaks exist in the magnitude of the magnetic field over the north pole (if vector components are considered, the maximum at 270° east longitude is the true "dip" magnetic pole). Likewise, there are two minimums near the equator; the largest of these is responsible for the so-called South Atlantic Anomaly, a region critical in determining radiation exposure in LEO. Finally, it should be noted that geomagnetic storm variations are superimposed on this main field. These are typically less that 0.01 G so that even during a severe geomagnetic storm, magnetic fluctuations are small at low altitudes compared to the average field (even though this is a very small change in the Earth's field, the effect of geomagnetic storms on particle fluxes in the polar ionosphere can be tremendous). However, they are critical at geosynchronous orbit, where the main magnetic field is of comparable strength, and dominate the magnetic field at higher altitudes.

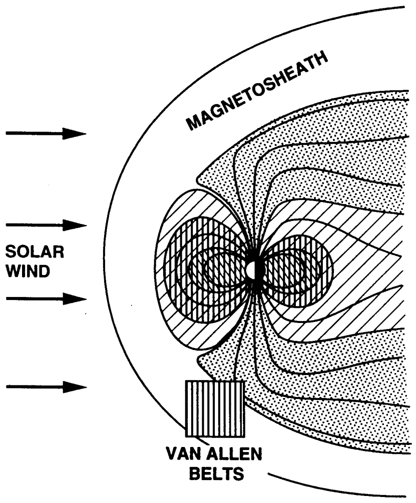

Figure 10a — Cross section of the Earth's magnetic field in the noon-midnight meridian

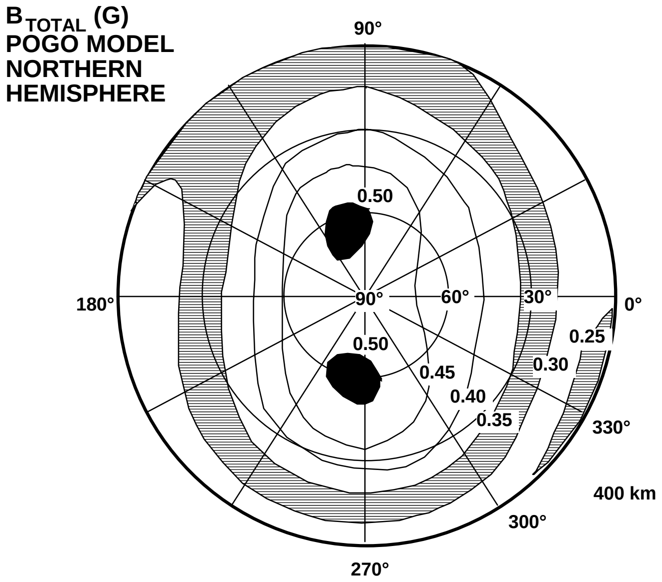

Figure 10b — The magnetic field amplitude over the northern hemisphere at a constant altitude of 400 km

3.3 Magnetic and Electric Field Effects

To understand the trapped radiation environment, one must first understand how charged particles move in the Earth's magnetic field. This section provides a very brief overview of the fundamentals of charged particle motion so that the concepts used in modeling the radiation belts can be comprehended. The reader is referred to many excellent texts in this area, such as the book by Roederer.[2]

3.3.1 Basic Particle Motion

To understand how charged particles become "trapped," it is necessary to review the forces that act on those particles. In general, except near the upper fringes of the Earth's atmosphere (<100–150 km), collisional and frictional forces on charged particles can be ignored. The two main forces (F_E and F_M) are then the electrostatic force:

$$\overline{F}_E = q\overline{E} \tag{11}$$

and the magnetic (Lorentz) force is:

$$\overline{F}_M = \frac{q}{c}\overline{V} \times \overline{B} \tag{12}$$

where q is the particle charge (including sign), c the speed of light, V the velocity vector of the particle, B the magnetic field vector in space, and E the electric field vector in space.

Consider the actual motion of a particle subject to Eqs. (11) and (12). Setting the electric field to zero and using the definition of the cross product, Eq. (12) implies that the force on a charged particle is always perpendicular to both its instantaneous velocity vector and the magnetic field vector. This means that a particle must, in the absence of another force and in the presence of a uniform magnetic field, move in a circle in the plane perpendicular to the magnetic field vector. It may additionally move freely (without any acceleration) along the magnetic field, mapping out a helix around its center of motion (Figs. 11–13). The radius R_c (called the cyclotron or gyro radius) of this circle is found by equating the centripetal force mV^2/R to the Lorentz force. In this expression, m is the particle mass and $V_\perp$ is the component of the velocity perpendicular to B. The expression is (relativistic):

$$R_c = \frac{\gamma m_0 V_\perp c}{qB} \tag{13}$$

The frequency with which the charged particle gyrates, the cyclotron frequency, ω_c is given by (relativistic):

$$\omega_c = \frac{qB}{\gamma m_0 c} \tag{14}$$

where ω_c is in radians per second.

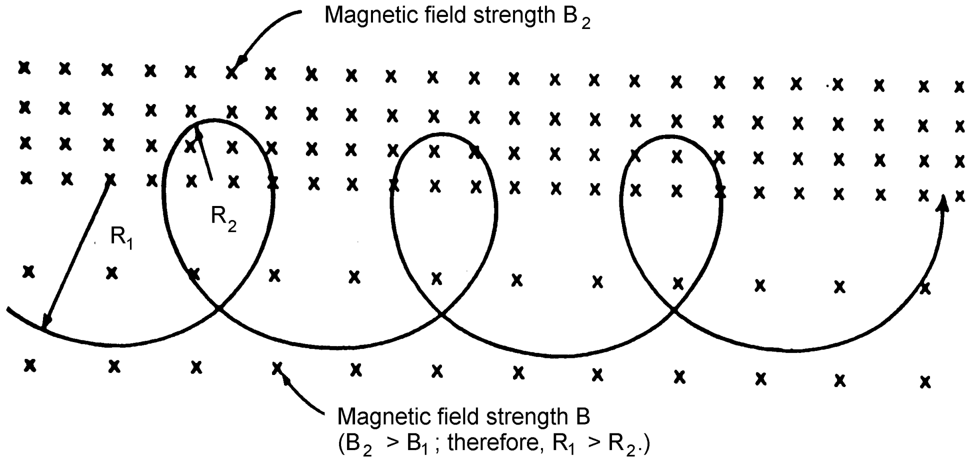

Figure 11 — Motion of a charged particle (positive in this case) in a magnetic field in the absence of an electric field

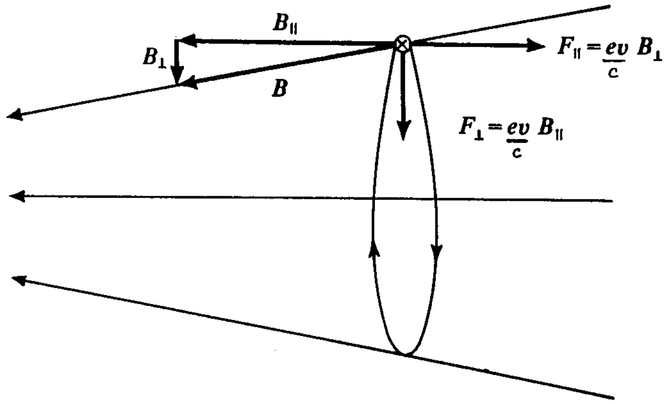

Figure 12 — Motion of a charged particle in a converging magnetic field in the absence of an electric field. F_1 is the force along the magnetic field that results from the field convergence (or divergence) and is responsible for the mirroring effect

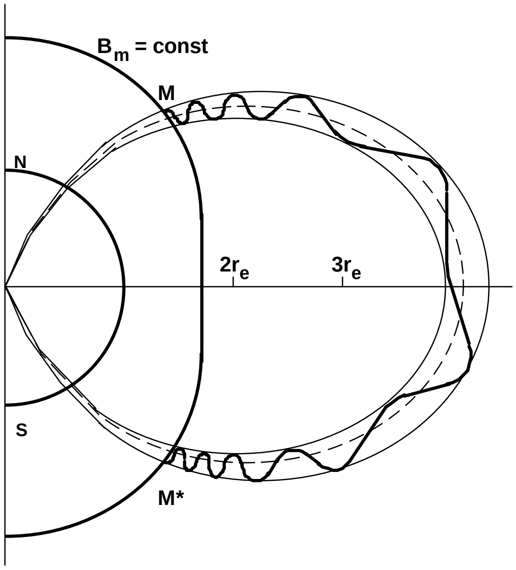

Figure 13 — Motion of a charged particle in a dipole magnetic field

According to Eq. (12), any particle motion parallel to *B* is unaffected by *B*. The particle's motion can be described in terms of a velocity parallel to the field $V_{||}$, or perpendicular to the field $V_{\perp}$, and a quantity called the particle pitch angle α, the angle the particle motion makes relative to the *B* direction. It is defined as:

$$\alpha = \sin^{-1}\left(V_{\perp} / V\right)$$

$$\alpha = \cos^{-1}\left(V_{\|} / \mathrm{V}\right) \tag{15}$$

The motion of the particle can be pictured as spiraling along the magnetic field direction, executing cyclotron motion around the field while moving along the field (Fig. 13). A charged particle will deviate from these simple motions if there is an electric field or if the magnetic field has temporal changes or gradients. As an example, consider the case when the magnetic field increases with distance in a direction perpendicular to the direction of *B*. In this case, as the particle moves from the region of low field strength to high field strength and back again, R_c decreases and increases correspondingly, and the particle traces out a cycloid configuration (Fig. 11). Under the combined influence of both the Earth's electric field (this field is radially directed close to the Earth and points from dawn to dusk at greater distances) and the radial gradient of its magnetic field, charged particles will slowly trace a similar cycloid around the Earth (electrons drifting toward the east and high energy ions toward the west). Although such motion is quite complex, if the magnetic field gradient *E* is sufficiently weak, the motion of the particle can be described in terms of its cyclotron motion and a constant drift velocity.

The final type of motion of interest here results from gradients along the magnetic field and is responsible for trapping radiation particles in the magnetic field. If the magnetic field converges, then the particle will feel a small force along the direction of the field line—which will cause the particle to decelerate (accelerate) as it moves into the converging (diverging) region (Fig. 12). Eventually (unless the particle has collisions with atmospheric particles—i.e., the mirror point is below some critical altitude, which we will define by the magnetic field strength at that position, B_c), the particle will have its motion parallel to the field stopped. However, due to the particle's circular motion (perpendicular to the field), it still experiences the decelerating force, which reflects the particle back along the field line. This occurs at the mirror point B_m, as determined by the strength of the magnetic field (Fig. 13). As will become evident, B_m and B_c are critical in determining charged particle motions.

3.3.2 Invariants of the Particle Motion

The many different types of motion of a particle in combined *E* and *B* fields initially appear to be very difficult to handle. In fact, if the *E* and *B* fields are changing rapidly in time and space in comparison to the characteristic motions of the particle, then careful, single particle trajectories must be calculated for each and every particle. Fortunately, the Earth's *E* and *B* fields generally change very slowly in time and space compared to the characteristic motions of radiation particles. We can then describe the particles' group motions in terms of so-called characteristic invariants of the motion (realizing that they do indeed change slightly) rather than having to calculate each particle trajectory. The adiabatic invariants help determine the scale over which the approximations hold. This section will describe those characteristic constants.

First, consider the cyclotron motion of a particle. The motion of a particle in a slowly varying *B* and *E* field can be described as a cyclotron motion superimposed on a slow drift of the particle's guiding center, the center of the cyclotron gyration. The energy and angular momentum of a charged particle will remain constant during this motion if the adiabatic invariants are conserved. The first adiabatic invariant, which represents this, is given by (relativistic):

$$\mu = \gamma^2 \left[\frac{m_0 V_\perp^2}{2B} \right] = \text{const} \tag{16}$$

μ is also called the magnetic moment invariant because it is equal to the magnetic moment of the charged particle ($\mu = IA$, where I is the current and A is the area of the loop). If the magnetic field changes slowly, the magnetic moment is conserved, and the ratio of the particle energy perpendicular to the field will stay constant relative to the magnetic field strength.

Equation (16) can be written in a useful equivalent form—a particle that mirrors at a field strength of B_m has a pitch angle at an arbitrary B ($B_m \geq B$) given by:

$$\sin^2(\alpha) = \frac{B}{B_m} \tag{17}$$

Consider the dipole magnetic field of the Earth [see Eq. (8)]. This field can be crudely represented by a tilted dipole with components:

$$B(r) = \frac{-2M \sin(\lambda)}{r^3} \tag{18}$$

$$B(\lambda) = \frac{M \cos(\lambda)}{r^3} \tag{19}$$

$$B(\phi) = 0 \tag{20}$$

where M = 0.311 G·R_e^3, R_e is the Earth's radius (1 R_e = 6371 km), and r is the radial distance from the center of the Earth; $B(r)$, $B(\lambda)$, and $B(\phi)$ are the field components in polar coordinates (note: λ = 90 deg – θ). For reference, a field line for this dipole field is defined by:

$$r = r_0 \cos^2 \lambda \tag{21}$$

$$\phi = \phi_0 = \text{const}$$

where r_0 is the radial distance at which the field line crosses the magnetic equator and a field line is the line that would be traced by always moving in the direction of the B vector.
The dimensionless quantity L can be defined where:

$$L = \frac{r_0}{R_e} \tag{22}$$

By the definition of r_0, the value of L is the equatorial crossing point of a magnetic field line in terms of R_e. Referring back to the discussion of the effects of a converging magnetic field, if the cyclotron radius is sufficiently smaller than the curvature of the Earth's magnetic field lines, then, to a good approximation, the case of a particle moving back and forth between two magnetic mirrors is as illustrated in Fig. 13. The particle does not move along a surface of constant B, but moves on a surface of constant L between M and M^* where $B = B_m$ in the northern and southern hemispheres.

L is important in defining the second invariant, called the longitudinal invariant. The second invariant Φ is defined by:

$$\Phi = \oint p_{\|} \mathrm{d}l = 2p \int_{M*}^{M} \left[1 - \frac{B(l)}{B_m}\right]^{1/2} \mathrm{d}l \qquad (23)$$

It is a constant of the particle motion (d*l* is a unit of length along the particle trajectory, and the second integral is between surfaces of constant B_m, e.g., *M* and M^*). *p* is the (relativistic) particle momentum, and $p_{\|}$ is the (relativistic) momentum along the magnetic field direction. Constant Φ means that as a radiation particle drifts, it traces out a cycloid around the Earth's equator and follows a well-defined surface between the mirror points at B_m. This surface defines the *L* shell of the particle; it means that a particle's trajectory can be completely defined simply by knowing its characteristic B_m and *L* values. This fact has given rise to the use of the McIlwain *B–L* coordinate system in which a particle population is described in terms of the particle flux as a function of *B* and *L* values; this simplification is the fundamental underpinning of most existing trapped radiation models in use today.

Particles that have B_m values that fall below approximately 100 km are generally lost to the atmosphere by collisions with neutral particles so that frequently, when plotting particle distributions as a function of α, a gap in the flux is found near 0 and 180 deg (this is not always true, however, as seen later). This is called the particle loss-cone angle for obvious reasons.

Combining Eqs. (18–21), it can be shown that:

$$B(\lambda)/B_0 = \frac{\left(4 - 3\cos^2(\lambda)\right)^{1/2}}{\cos^6(\lambda)} \qquad (24)$$

B_0 is the total magnetic field value. The magnetic latitude, at which a particle with pitch angle α_o at the magnetic equator will mirror, can be determined by combining Eq. (24) with Eq. (17) to get:

$$\sin(\alpha_0) = \frac{\cos^3(\lambda)}{\left(4 - 3\cos^2(\lambda)\right)^{1/4}} \qquad (25)$$

This expression can be used to determine the maximum pitch angle that a spacecraft can see at a given latitude in space. That is, if the spacecraft passes through the magnetic field line at a magnetic latitude of λ, it can only detect particles that have equatorial pitch angles of α_o or less (for 0 to 90 deg). All particles with initial pitch angles greater than α_o at the equator will have mirror points that lie between the spacecraft latitude and the magnetic equator and, therefore, will not be detected by the spacecraft detectors.

The third invariant of the motion *Q* is the flux invariant. This is simply the net magnetic flux inside the longitudinal–invariant surface defined by:

$$Q = \int \overline{B} \cdot \mathrm{d}\overline{s} \qquad (26)$$

where d*s* is an element of area. This invariant implies that the guiding center of the particle follows slow changes in the Earth's magnetic field.

The three invariants together allow the development of simple time-averaged models of the radiation particle fluxes. It should be remembered, however, that perturbing electric and magnetic fields occasionally modify the particle motion so that the three invariants are violated. Perturbations in the magnetosphere occur on timescales of the cyclotron, the bounce, and the drift periods, which violate the three invariants and alter the particle motion. Such variations lead to the diffusion of the particle populations (primarily the electrons) in pitch angle so that the loss-cone can sometimes be filled with particles and also produce radial diffusion, resulting in a buildup of energetic electrons at lower altitudes.

4. AE8 and AP8 Models

There are potentially many different ways to model the Earth's radiation environment. Fortunately, the use of the above described adiabatic invariants and the introduction of the McIlwain *B–L* coordinates have led to a standardized means of representing the time-averaged features of the trapped radiation environment. Until the Combined Release and Radiation Effects Satellite (CRRES) mission, the AE/AP series of radiation models developed by Vette and his colleagues at NASA Goddard have been the principal source of a uniform set of practical models of the Earth's trapped radiation environment. Here, the major characteristics of the Earth's trapped radiation environment will be summarized in terms of these AE/AP models, with emphasis on the critical environmental variables. The AP8/AE8 models are based on compiled data from many different satellites.[15-17] The P and E in the model names AP8 and AE8 refer to proton and electron and 8 is the version number of the models. For a given set of McIlwain *B–L* coordinates in the range from LEO to somewhat beyond geosynchronous, AP8 and AE8 provide estimates of the omnidirectional fluxes of protons in the energy range of ~50 keV to 500 MeV and electrons in the energy range of ~50 keV to ~7 MeV. Time-dependent variations of the radiation fluxes such as those due to geomagnetic storms or short-term solar modulations are not included in AP8/AE8. However, the models differentiate between solar cycle maximum and minimum conditions. For protons, a larger flux is predicted at solar cycle minimum than at solar cycle maximum.

As discussed, a common procedure in modeling the radiation environment is one in which the omnidirectional flux of particles, integrated over an energy interval, is given as a function of *B* and *L* coordinates. By definition, omnidirectional means that the particle flux has been averaged over all pitch angles. Units are typically particles per square centimeter per second with the integrated energy channel being from a lower energy to the highest energies capable of being measured by space detectors. Although for specific cases, such as the shielding design for sensitive particle or light detector systems, pitch angle is important, in practice, the design community that uses these codes requires only the omnidirectional flux.

In principle, it is possible to construct this type of simple model by one measurement of the fluxes at all pitch angles as a satellite moves away from the Earth in the magnetic equatorial plane. The major difficulty in developing such a model of the Earth's radiation belts is that both space and time must be factored into the model. Although the use of the adiabatic invariants and *B–L* coordinates help simplify this task, in reality, asymmetries in the Earth's magnetic and electric fields and their time variations introduce significant complications into the modeling process. In particular, shell-splitting (particles of the same energy but with different pitch angles tend to follow slightly different drift paths around the Earth so that particles observed together at the equator on one side of the Earth are separated in radial distance on the other side), distortions in the Earth's magnetosphere, and similar effects force the inclusion of temporal and local-time (or, less precisely, longitudinal) variables. For example, the AE/AP model fluxes are parametrically represented by:

$$I(>E, B, L, \tau, T) = N(>E, L)\Phi(>E, L, \tau)G(B, L) \tag{27}$$

where I is the integral omnidirectional flux, $>E$ means for all energies above E, τ is the local time, and T is the epoch (or date). No individual spacecraft can collect sufficient data over a long enough time interval or in enough locations to adequately define Eq. (27). Rather data from many different satellites are averaged in discrete B and L bins to determine the B–L variation G; in energy, L, and local time to determine the local-time variation Φ (note: B variations were ignored because there were often too little data to allow simultaneous binning in terms of B); and in energy and L bins to determine the energy variations N.

Because many different satellites were used, it was important to know the efficiency and geometric factor for the different detectors.

Figure 6 for 1 MeV electrons and 10 MeV protons illustrates the basic structure of the radiation belts as predicted by the AE8 and AP8 models. The electron contours show a dual peak. Therefore, according to these models, the radiation belts are typically divided into inner zone and outer zone populations. This division also roughly corresponds, for the electrons, to an inner belt that is weakly affected by geomagnetic storms and an outer belt that is greatly affected by storms. The L-shell region up to L~2.5 is termed the inner zone, while the region beyond L~3 is considered to be the outer zone, with a “slot” region of reduced density in between. The inner zone electrons peak around $L = 1.45$ to 1.5. Little variation with geomagnetic activity is seen below L~1.6. The inner zone protons are very stable, varying inversely with atmospheric density (the fluxes are lower at solar maximum when the atmospheric density is highest) and solar cycle (cosmic rays have easier access to the vicinity of the Earth at solar minimum, resulting in increased CRAN decays). The proton flux peaks near $L = 1.45$. In the outer zone, the peak L shell varies with energy for the electrons, and flux increases can be as great as 10^5 in less than one day during a geomagnetic storm. The protons, in contrast, do not show a division into inner and outer belts nor do they show as much variation with geomagnetic activity. Protons with $E \geq 1$ MeV peak at about $L = 3$, while protons with $E \geq 10$ MeV peak at about $L = 2.5$. (Note: all numbers are adapted from Vampola.[18])

Below 1000 km, the main trapped radiation environment consists of two components: the low altitude extension of the radiation belts (or horns) at high latitudes and the low latitude South Atlantic (Magnetic) Anomaly. Figures 14 and 15 illustrate these regions for protons and electrons.[19] The units are particles/$\text{cm}^2\cdot\text{s}$ for $E > 30$ MeV and $E > 0.5$ MeV, respectively. The lines represent isoflux contours at 296 km (Fig. 14) and 400 km (Fig. 15). The South Atlantic Anomaly, which is the result of low magnetic field intensities in the South Atlantic near Brazil (Fig. 10), is slowly drifting westward with a period of about 1200 years.

To summarize, the AP8/AE8 models describe the following populations:

1) The slowly varying, stably trapped high energy protons and the inner zone electrons ($\leq 3\ R_e$). (Note: the AP8MAX and AP8MIN differ only for altitudes less than approximately 1000 km.)

2) The trapped but highly variable outer zone electrons ($\geq 3\ R_e$).

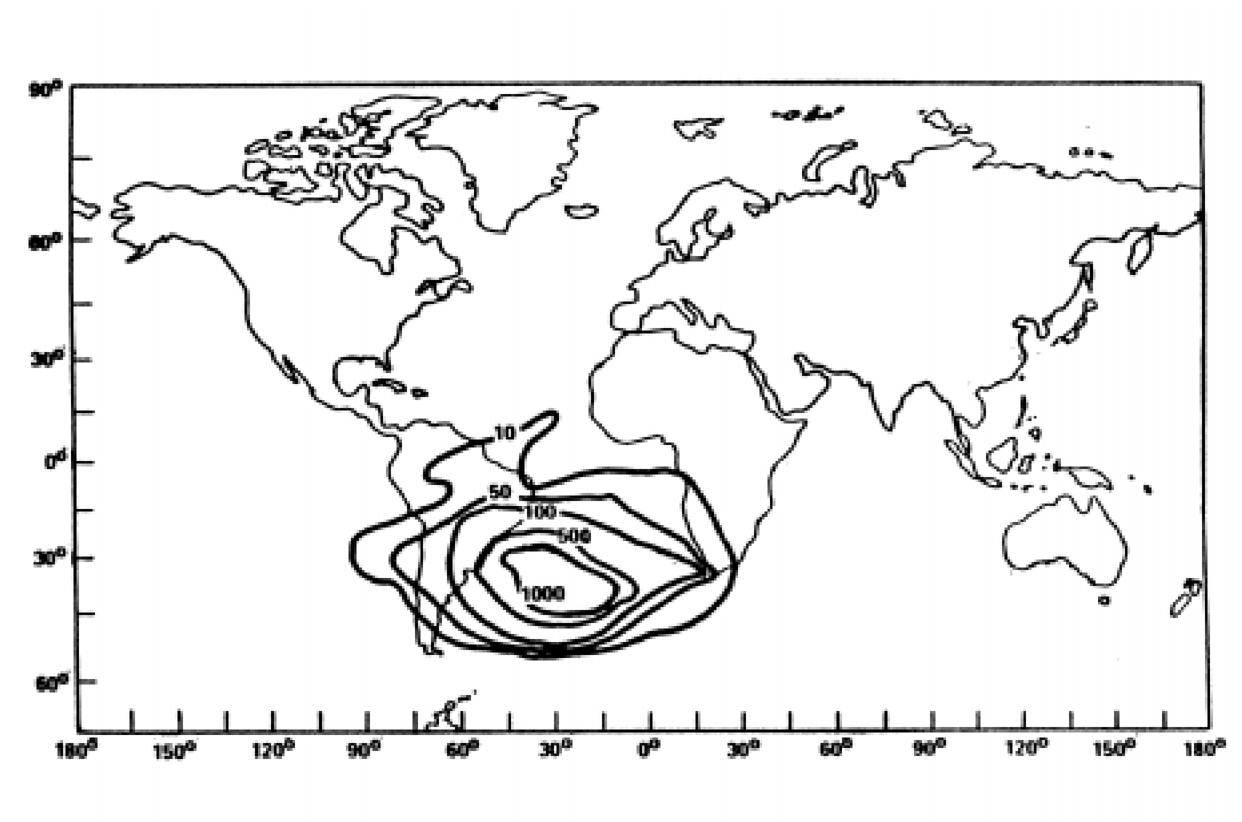

Figure 14 — Proton flux densities at 296 km altitude

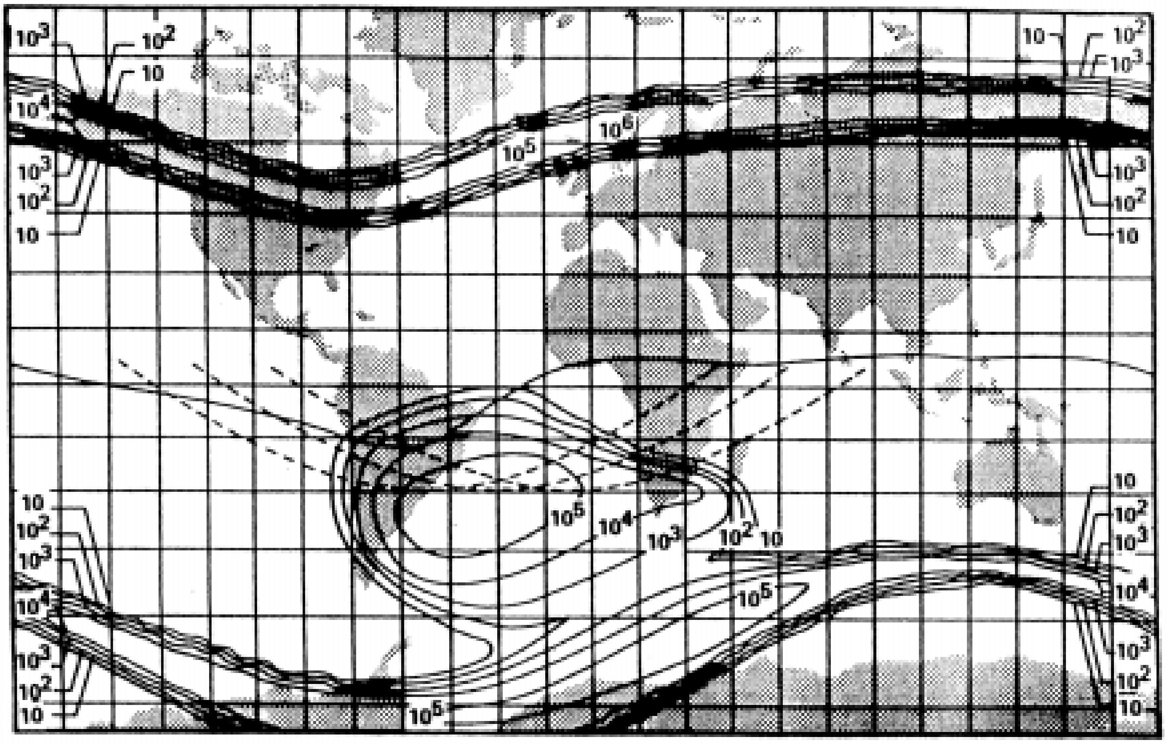

Figure 15 — Electron constant flux contours at 400 km altitude (*E* > 0.5 MeV)

5. Problems with AE and AP

Several difficulties arise in estimating the trapped radiation environment using the AE8/AP8 models. Of principal concern are the complications introduced by time variations in the plasma environment over the solar cycle and short-term geomagnetic storm effects. These effects currently complicate attempts to accurately characterize the radiation particle population in an “average sense” using AE8/AP8.

At low altitudes, the main problem with the AE8/AP8 models is the changing magnetic field necessary to compute the B,L coordinates. High energy, trapped particles mirror at a characteristic constant magnetic field strength; thus, particles that typically would mirror at higher altitudes above the atmosphere find themselves mirroring at much lower altitudes (e.g., the South Atlantic Anomaly), thereby enhancing the background fluxes. Because the Earth’s magnetic field is slowly changing, the B–L coordinates have been changing. At first, an attempt was made to simply update the magnetic field models used. This proved impractical, however, because the trapped fluxes were tied to the particular magnetic field model being used when they were determined. The short-term solution has been to use the magnetic field for the epoch in which the radiation model was developed. In the long term, however, the models will have to be overhauled and some means for incorporating the current magnetic field developed because the magnetic field is continuously changing. A new approach for modeling energetic protons at low altitude has been to describe their intensities in terms of the column-integrated atmospheric density encountered along their drift path.[20] This approach has been shown to produce valid results for low altitude orbits.[21]

The main issues at higher altitudes are two fold. First, the electron radiation flux is typically highly variable on a daily timescale—for example, some variations being on the order of 10–100 at geosynchronous orbit. Second, the AE model is biased toward a few major geomagnetic storms. This biasing is to be expected because the model is derived by averaging the fluxes. Inside L = 1.8 (generally referred to as the inner electron zone), the time variations are quite small, demonstrating the usefulness of an average model in this region at low latitudes. In contrast, outside L = 1.8, the fluxes vary greatly with time due to geomagnetic activity. However, the principal point to be made is that large time variations are observed but that long-term averages do indeed smooth out these variations so that average models are useful in many applications. An additional shortcoming of AE8 in the inner zone is that the data used to generate the model were contaminated by fission electrons from the Starfish exoatmospheric nuclear test.[22,23]

Although a given AE/AP model may be accurate for the period of time during which the measurements were taken, it does not necessarily follow that it is accurate for another epoch. That is, there are long-term variations such as the decay of the Starfish nuclear explosion radiation that change over much longer timescales than data exist. The solar cycle, for example, follows an irregular 11-year pattern and the level of geomagnetic activity at one solar minimum may differ substantially from that of the next. Thus, for a model to be appropriate for a given time interval, it should ideally include observations from that interval. Because this is impossible in practical terms, the data base used should be as close in time as possible if accurate predictions are to be expected. The most recent observations for the AE models (and these are principally from one satellite) are more than 15 years old, whereas for the AP8 model they are almost 20 years old!

5.1 Solar Cycle Effects, Storms, Substorms

Figure 16 illustrates approximately one year’s worth of hourly averages of the 1.9 MeV omnidirectional electron flux measured at midnight by the geosynchronous satellite ATS 1.[24] The daily sum of the geomagnetic index K_p (at the bottom of the figure) and the values predicted by the AE model (the horizontal line) are also plotted for comparison. The horizontal line is the AEI-7 model equatorial flux at L = 6.6 and local midnight. This figure demonstrates two points discussed earlier: the high daily variability of the geosynchronous orbit (as mentioned, factors of more than 100 are clearly visible) and the bias toward the few major geomagnetic storms.

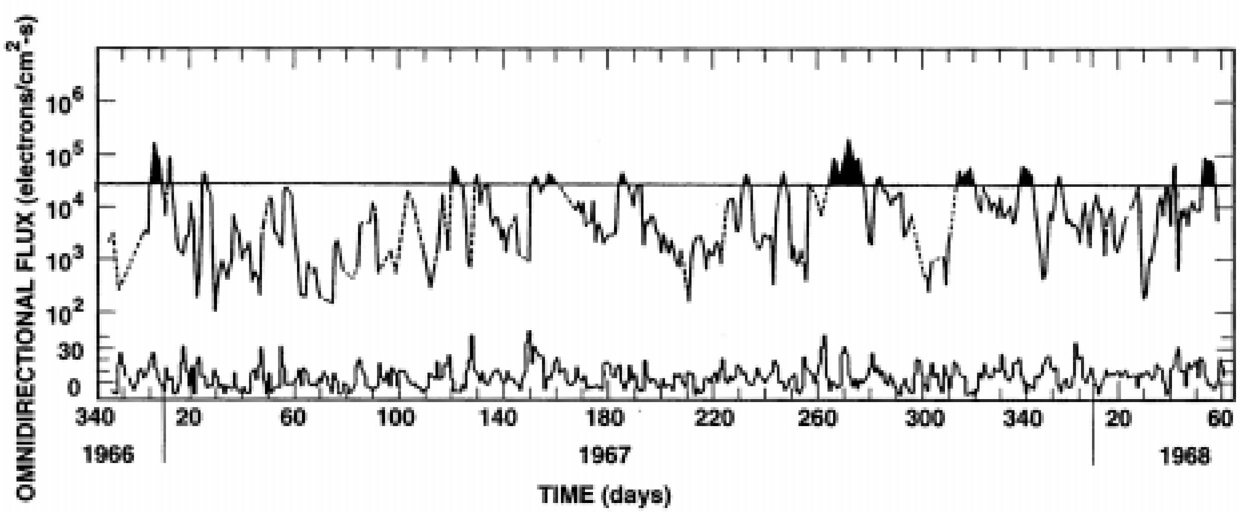

Figure 16 — Hourly averages of ATS 1, 1.9 MeV omnidirectional electron flux at local midnight (Copyright by and used by permission of American Geophysical Union)

Figure 17 demonstrates electron variations over a slightly longer time period for different *L* values. The data are 10-day averages of the electrons with energy greater than 0.28 MeV, taken on the 1963 38C spacecraft.[24] Inside *L* = 1.8, the inner electron zone, the time variations are quite small. The steady decay of flux levels in the inner belt is due to the decay of the residue from the artificial Starfish injection event of July 1962. The figure also illustrates how geomagnetic activity has an increasing effect on the fluxes at higher *L* shells (*L* = 2.2 in the figure).

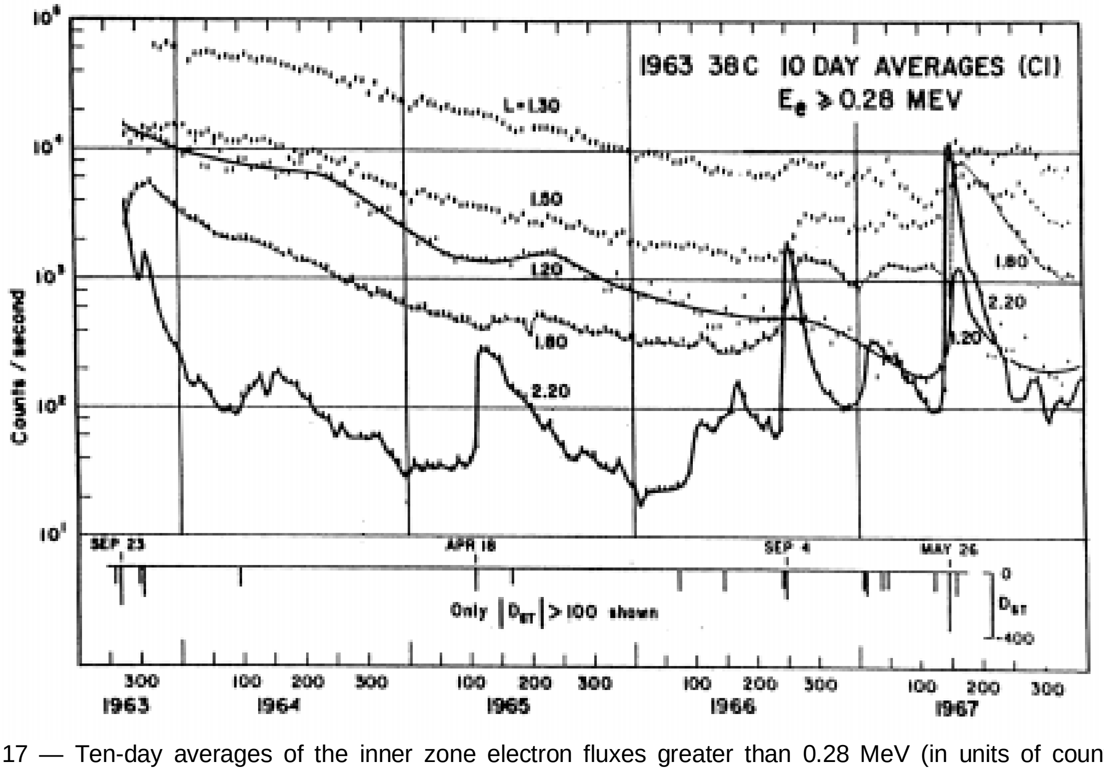

Figure 17 — Ten-day averages of the inner zone electron fluxes greater than 0.28 MeV (in units of count rate) measured by the satellite 1963-38C (Copyright by and used by permission of American Geophysical Union)

As a final example of long-term variations, consider Fig. 18.[25] This plot presents running 27-day averages of omnidirectional electron fluxes at geosynchronous orbit during a solar cycle. Energy channels (in MeV) are indicated along with the corresponding satellite (all are geosynchronous). The fluxes are remarkably stable over this period if sufficiently long averages are taken.[25] The most pronounced variations in the figure are those associated with an apparent semi-annual variation. Paulikas and Blake[25] also found a strong correlation between solar wind velocity and the energetic electron fluxes. However, the principal points to be made by this and the previous figures are that large time variations are observed in the outer electron zones but that long-term averages do indeed smooth out these variations so that average models are useful in many applications.

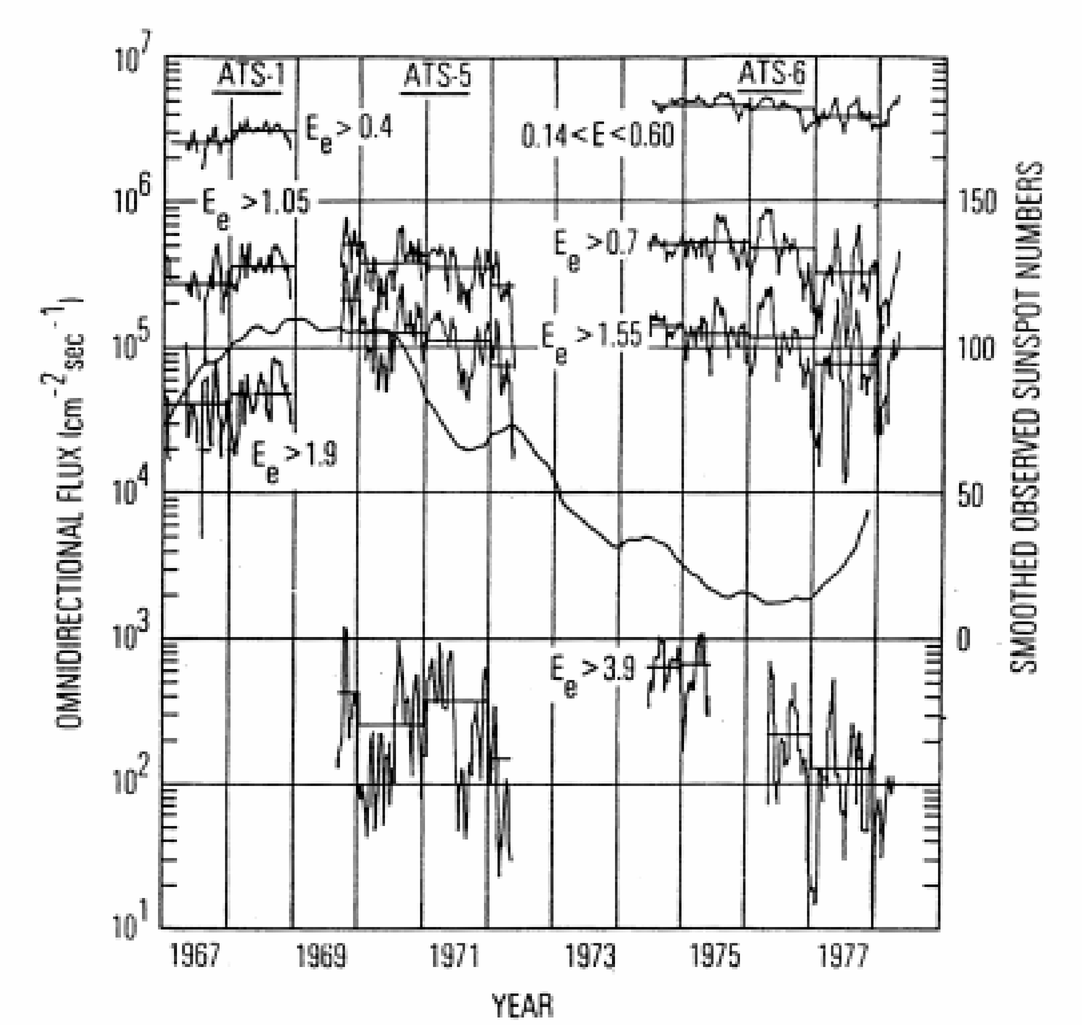

Figure 18 — ATS 1, ATS 5, and ATS 6 energetic electron fluxes as a function of time. ATS 5 data were normalized to ATS 6 data in mid-1974. The energetic thresholds for the ATS 1, ATS 5, and ATS 6 channels are shown in the figure. The flux averages for each year are also indicated (solid horizontal lines). The Zurich monthly sunspot numbers are superimposed on this graph. (Copyright by and used by permission of American Geophysical Union)

5.2 Examples: Loss-Cone and Field-Aligned Distributions

Because the pitch angle distribution at one point on a field line in principle gives information on the plasma distribution at other locations along the field line, it is important that this function be properly defined. This is not straightforward because it is difficult in practice to accurately determine the pitch angle distribution. Indeed, in practice, spacecraft are seldom at the magnetic equator nor are they able to sample all pitch angles. Furthermore, particles are observed with pitch angles along the magnetic field direction in the loss-cone. These particles are believed to be produced by nonadiabatic processes and thus violate the basic principles on which the time-averaged radiation models are based. The issue that arises is what are acceptable limitations on the pitch angle distribution?

Figure 19[26] presents examples of electron pitch angle (α) distributions. Although these measurements are from a geosynchronous spacecraft, the observations hold for *L* shells throughout the magnetosphere (e.g., see examples from Explorer 45[27,28] that cover electron and proton pitch angle distributions from *L* shells of 1.7–5.2). The left-hand and center panels show a pronounced field- aligned distribution (sometimes called a cigar-shaped distribution) with only a weak loss-cone along the magnetic field line (α = 90 deg). The right-hand panel from 2 hours later shows a strong loss-cone as expected for trapped particles—indeed, this is a so-called pancake distribution. Clearly, the variations in particle pitch angle distributions are quite complex at all energies and vary greatly with *L* shell. Given the sharply field-aligned fluxes on some occasions and the pronounced loss-cone distributions on others, it is clear that interpolation of the pitch angle distribution from a limited data set can be a difficult undertaking. The fact that the pitch angle distribution can change over the course of a geomagnetic storm and that it can vary drastically with energy greatly increases the number of measurements that must be made and the time intervals over which data must be taken.

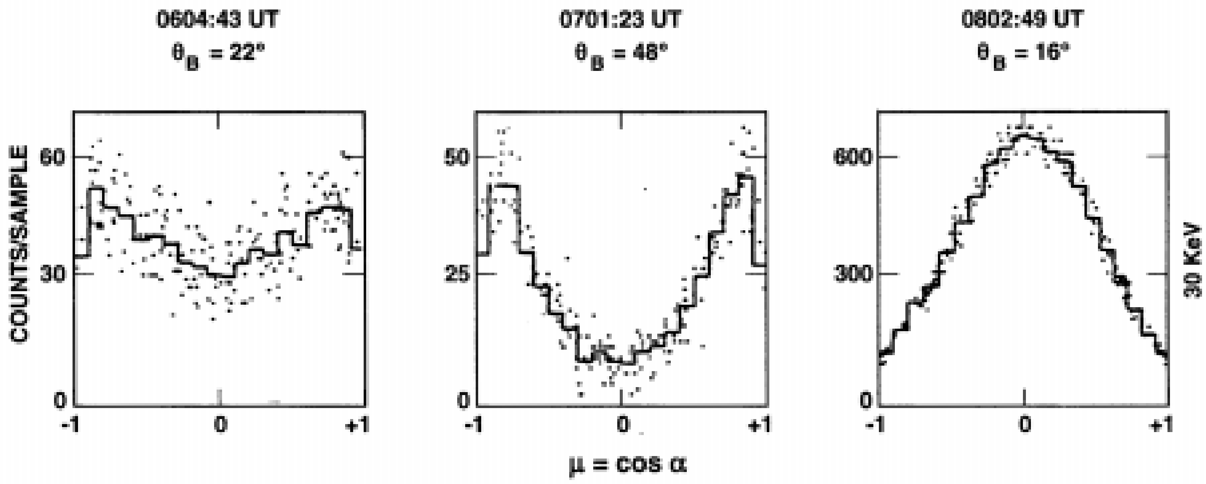

Figure 19 — Pitch angle distributions observed at selected times during the geomagnetic substorm of September 8, 1977

5.3 Coverage Limitations

In addition to the limitations associated with temporal and pitch angle variations, the AP/AE models are limited by coverage. Specifically, existing models are affected by lack of adequate coverage at some pitch angles and by lack of coverage during the current epoch. These limitations are illustrated in Fig. 20.[15] Here, the B/B_0–L coverage for the experiments used in constructing the AP8 model is illustrated. The model and the data used have been cutoff at *L* = 6.6. As is demonstrated, that coverage can be quite limited, and over many ranges may be measured by only one satellite. To address these issues and bring the radiation data base up to date, the CRRES spacecraft was launched in 1990 to remap the radiation belts and to study radiation effects on microelectronics. The results of the one year mission of the CRRES clearly revealed problems with current models. It also produced detailed measurements of a shock-induced highly energetic (*E* > 15 MeV) electron transient belt in the slot region.[29] Results from CRRES will be discussed further in Section 6.

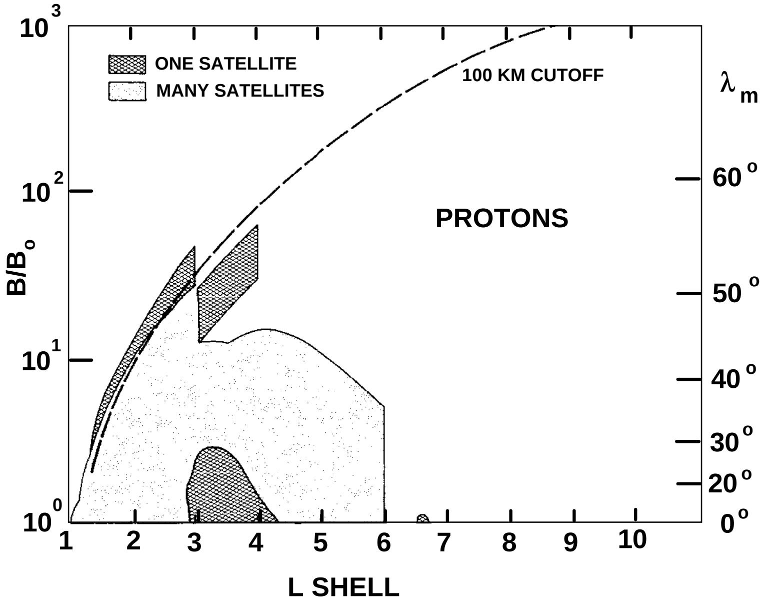

Figure 20 — *B/B_o-L* coverage for experiments used in constructing the AP8 model

5.4 AE8/AP8—The Design Issues

Not only do the AE8/AP8 models drive the selection of parts and the design of shielding, but they also form the backdrop against which mission optimization is carried out. Errors (either conservative or the opposite) in estimating the radiation environment can have a substantial economic impact through excessive shielding mass or early satellite loss. Thus, it is critical from the start to have access to the best estimates of the ambient radiation environment. In addition, the space community is reluctant to change to newer models because of the long history attached to the AE8/AP8 and related models. Any change to newer models will require a demonstration of both the benefits over and expected changes from the older models.

It must be realized that any quantitative estimates of the inaccuracies in the current trapped radiation models are very crude because such estimates are intimately tied to the issue of what the models are to be used for. At best, estimates of these inaccuracies are made based on comparisons between the levels of dosage that the models would predict for a given orbit and the actual levels measured in that orbit. Vampola[30] has attempted such estimates and finds the models to be within a factor of 2 for long time averages (for 5- to 10-year averages) of the observed results:

AP8:	(min. and max.):	a factor of 2
AE8:	(min. and max.):	a factor of 2

The improvements in sizing satellite shielding that can be expected with better models cannot be underestimated; this can be graphically demonstrated (in both senses of the word) by a simple parametric comparison. Figures 21 (protons) and 23 (electrons) show the range in flux as a function of energy spectrum shape expected, based on the current uncertainties in the radiation environment,[31] and the resultant effects on the shielding for both protons (Fig. 22) and electrons (Fig. 24). As a practical example, improvements in the knowledge of just the slope of the electron spectrum for energies greater than 2 MeV might mean perhaps as much as an order of magnitude reduction in the required shielding on a typical spacecraft (although factors of 2 are more likely), if it could be demonstrated that the softer spectra were more appropriate for a long mission.

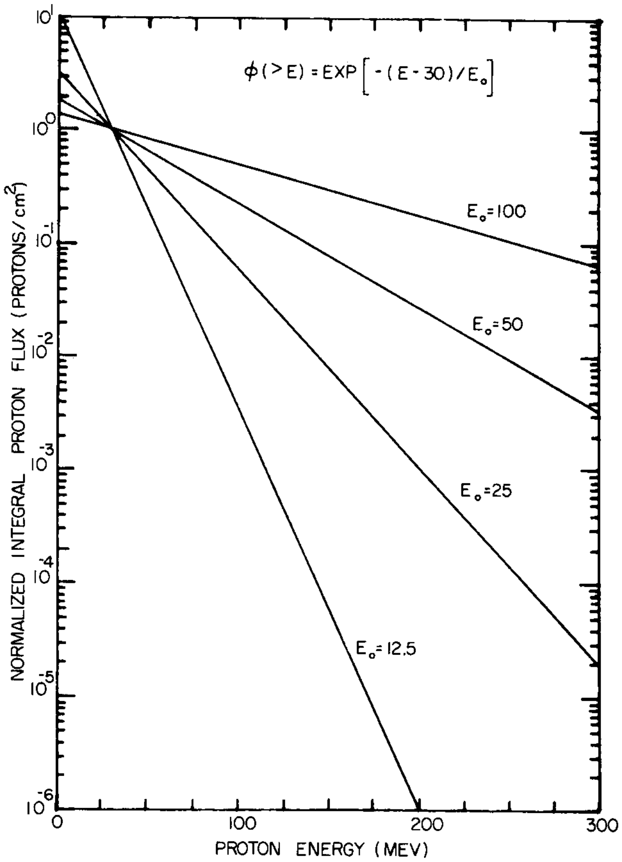

Figure 21 — Normalized integral proton flux as a function of proton energy (Copyright by and used by permission of American Geophysical Union)

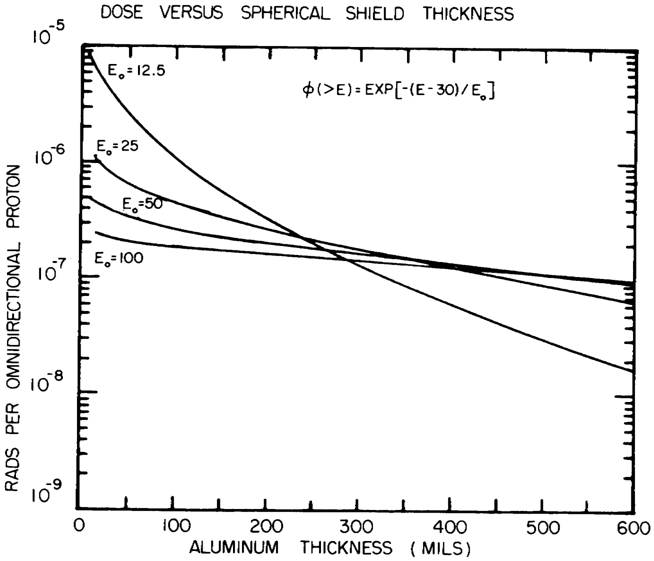

Figure 22 — Depth-dose per omnidirectional proton as a function of spherical aluminum thickness (Copyright by and used by permission of American Geophysical Union)

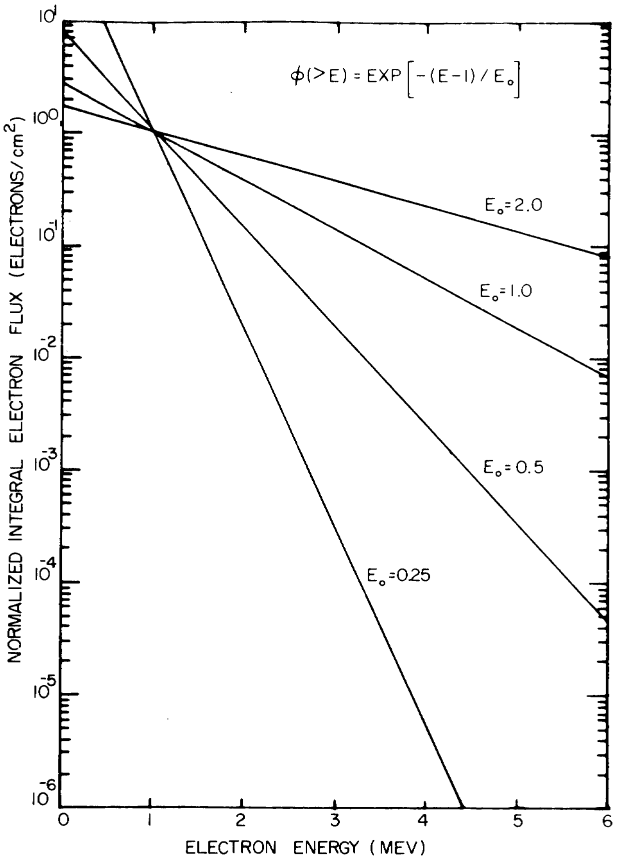

Figure 23 — Normalized integral electron flux as a function of electron energy (Copyright by and used by permission of American Geophysical Union)

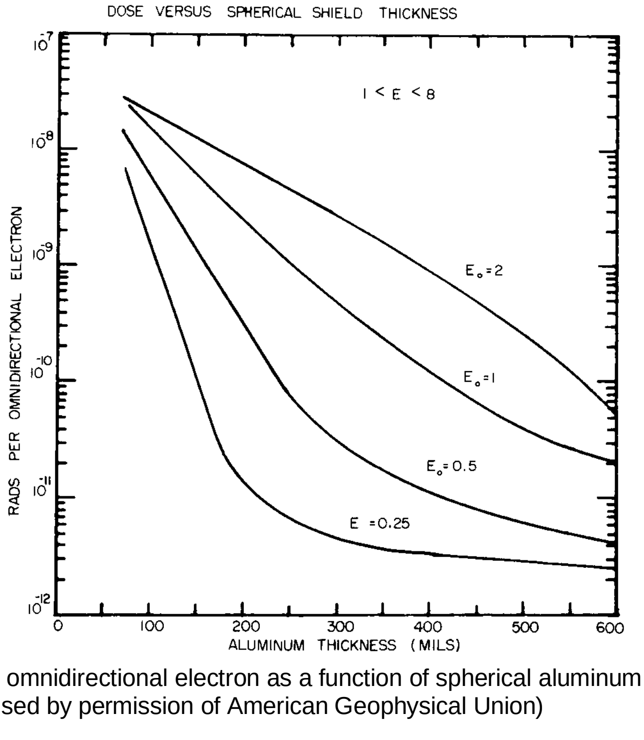

Figure 24 — Depth-dose per omnidirectional electron as a function of spherical aluminum thickness (Copyright by and used by permission of American Geophysical Union)

6. Current Radiation Modeling Efforts

The radiation modeling community is presently in a state of flux. The older models of the radiation environment are being revised as new data become available. Three environments need to be considered in modeling the trapped radiation environment. First, there is the trapped radiation environment itself. For the past two decades, it has been primarily modeled using the NASA Goddard AE8/AP8 flux models and associated magnetic field models. Superimposed on this environment is that due to cosmic rays and to solar proton events (often inaccurately termed solar flares). These environments have been characterized by the Naval Research Laboratory (NRL) (primarily Jim Adams and his colleagues). Both sets of models are showing their age, however, and a series of new models and discoveries is leading to their modification (note: new versions of the NRL CREME codes have recently become available and can be accessed over the Internet). These changes can be summarized briefly as:

1) The new CRRES data. The CRRES satellite recently made measurements of the inner radiation belts. These data have been combined into several radiation models, one of which is CRRESRAD. However, the CRRES data are supposed to adequately cover only the ±40° latitude band.

2) The JPL solar proton model. JPL has developed a new model of the solar proton fluences. The model is currently very popular with mission planners because it properly accounted for the 1989 range of extreme fluxes. It will not be further discussed here.

2) The new, heavy ion belt. Both Russian and U.S. spacecraft have recently detected a new, heavy ion belt at low latitudes that could affect ICs. It is still being defined, however, and is apparently very dependent on solar cycle. Anomalous cosmic rays are believed to be the primary source of this belt, which varies with solar cycle.

4) JPL low energy inner zone proton model. This model covers the energy range 80 keV to 3 MeV for altitudes up to 8000 km. It was generated from data obtained by the S3-3 satellite in the mid-1970s and exhibits fluxes as great as 3 orders of magnitude higher than AP8 for $E < 1$ MeV and $L < 1.6$. In the AP8 model, fluxes less than 5 MeV are extrapolations from higher energies. The JPL model has been confirmed with data obtained by the AZUR-4 satellite in 1968 and data obtained by the Russians on Molniya satellites in the 1970s.[32]

6.1 CRRES Models

Given the many known uncertainties in the AE/AP models, the DoD (primarily the Air Force Research Laboratory) and NASA launched an aggressive program in the 1980s to address many of their shortcomings. This resulted in the CRRES program. CRRES was launched on 25 July 1990 and ceased transmitting on 12 October 1991. It was placed in an 18.1 deg, 350 by 33,000 km orbit with a period of 10 h. The satellite carried perhaps the most complete complement of radiation environment sensors yet flown and was in a nearly ideal orbit for mapping the trapped radiation belts. Approximately 14 months of data were obtained during solar maximum before a battery failure terminated the mission. The data have been used to develop several new models of the trapped radiation environment and to test the AE/AP models. The results of these studies have been reported in a number of recent papers by the Air Force Research Laboratory and others.[33–35] Two of the trapped radiation models developed by the Air Force Research Laboratory (CRRESRAD[33] and a quasi-static model of the outer zone electrons[34]) will be briefly reviewed in this section.

The CRRESRAD model[33] is a readily accessible PC-based software program that provides estimates of the dose behind four shielding thicknesses for a large range of satellite orbits. The model is based on the Space Dosimeter experiment,[36] which returns dose data in the energy ranges 50 keV–1 MeV (LOLET) and 1–10 MeV (HILET). The dose is measured behind four thicknesses of hemispherical aluminum shielding (0.57, 1.59, 3.14, and 6.08 gm/cm^2). These correspond to electrons with energy greater than 1, 2.5, 5, and 10 MeV and protons with energy greater than 20, 35, 52, and 75 MeV. To create a model, the data were divided into two parts: a “quiet period” before the March storm (27 July 1990–19 March 1991) and an “active one” after the storm (31 March 1991–8 October 1991). The data were then averaged in *L* and B/B_O bins (where B_O is the amplitude of *B* at the magnetic equator for the given value of *L*). Separate tables were then computed for the two time periods, for the total period, for the LOLET and HILET and LOLET + HILET channels, and for the four shield thicknesses. This resulted in 36 dose tables. To determine the dosage expected for a specific satellite orbit, the code integrates the electron and proton dosage (interpolated from the appropriate tables for a given shielding) along the orbit for quiet, active, or average geomagnetic activity conditions.

Sample data for the CRRESRAD model are plotted in Figs. 25 and 26.[35] These results are for the dose rate, in Rad(Si)/s, as a function of *L* along the magnetic equator. The data are plotted in terms of HILET (for protons >20 MeV) and LOLET (>2.5 MeV electrons and >135 MeV protons) for the quiet and active models and for a comparable calculation using the AE8 and AP8 models. The figures illustrate the differences between the CRRES and AE/AP models.

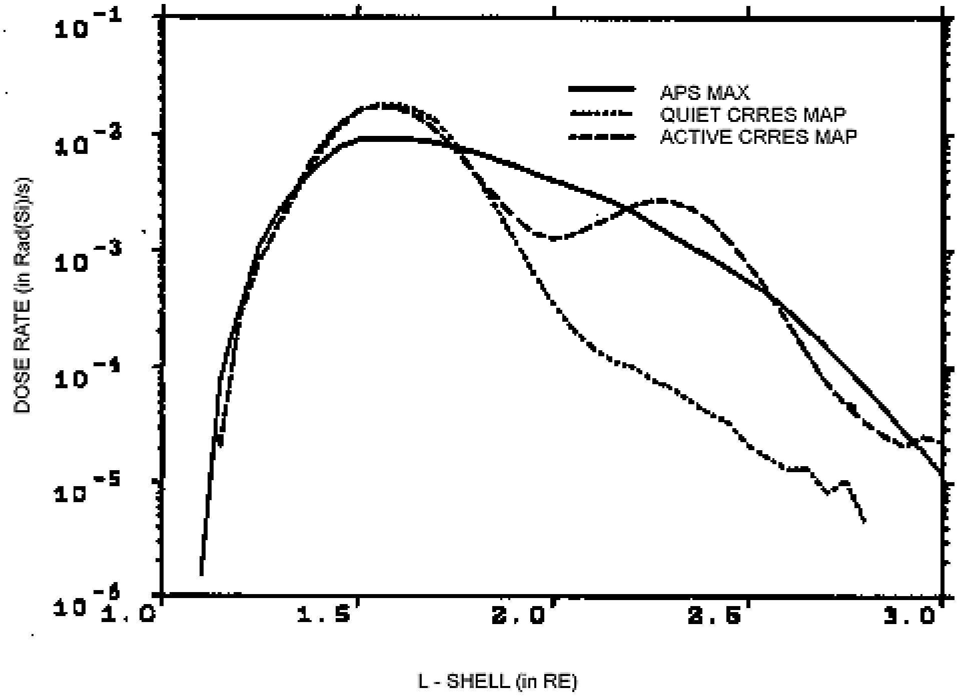

Figure 25 — Comparison of dose rate along magnetic equator as a function of *L* for quiet and active CRRES dose models and for AP8MAX.
(Copyright by and used by permission of the Committee on Space Research)

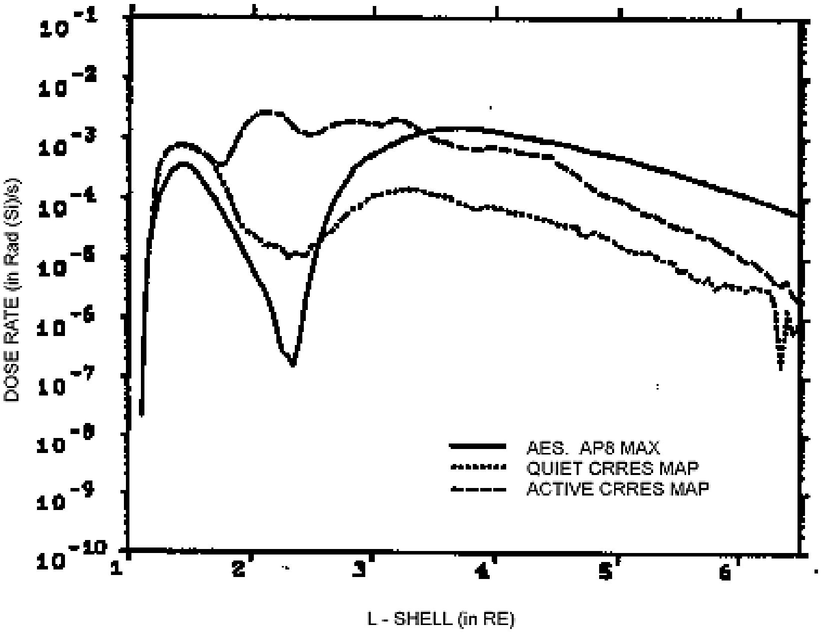

Figure 26 — Comparison of dose rate along magnetic equator as a function of *L* for quiet and active CRRES dose models and for AP8MAX/AE8MAX.
(Copyright by and used by permission of the Committee on Space Research)

Specifically, in Fig. 25, there is relative agreement between the active CRRES model and the AP8 model for $E > 20$ MeV protons, whereas the low activity CRRES model is about an order of magnitude lower in dosage for $L > 2$. At higher energy cutoffs, this difference is reversed with the AP8 model agreeing more closely with the quiet model and being an order of magnitude lower than the active model for $L > 2$. These differences are explainable in terms of a second, variable proton belt extending between $L = 1.8$ and $L = 4$ present in the CRRES active model that is not present in the AE/AP models.

For Fig. 26, there are much larger differences among the models. In particular, the AE/AP model results exceed the CRRES models for $L > 3.5$ (primarily because of the >2.5 MeV electrons) and is lower for $L < 2.5$. In fact, differences of three orders of magnitude exist between the active model and 1.5 orders between the quiet model and the AE/AP model in the slot region near $L = 2.5$. This is probably due to the absence of electrons above 5 MeV in the AE8 model and their presence in the CRRES models. Other differences exist among the models, but these figures illustrate the major concerns—namely the extra proton belt in the CRRES active data and the lack of high energy electrons in the NASA models. The implications of these and other differences among the models for mission designers need to be carefully considered.[34,35]

The second model is the quasistatic model.[34] In this model, data from the CRRES high energy electron fluxmeter (HEEF), a particle detector that measures electrons in 10 different energies between 0.8 and 8 MeV, were used to construct a quasistatic model of the outer zone electrons based on the A_p index. The intent of the model is to provide a more accurate representation of the dynamic behavior of the outer zone. The CRRES spin axis points toward the sun, while HEEF points perpendicular to the spin axis. Averaging over a satellite spin gives an estimate of the unidirectional electron flux at a given *L*. Brautigam et al.[34] found that these fluxes were approximately correlated with the logarithm of a 15-day running average of the A_P index lagged by 1 day (called A_{P15}). They then computed average radiation belt profiles as functions of *L* (between 2.4 and 6.6) energy (nine of the energy channels between 1 and 8 MeV) and for A_{P15} (eight intervals between 5 nT and 55 nT). A typical result for one of the energy channels (3.09 MeV) is presented in Fig. 27[34] and is compared with a corresponding prediction based on the AE8MAX model. The figure illustrates a basic conclusion of the Brautigam et al. study, showing that the AE8 model is typically higher than the CRRES measurements at all *L* values above ~3.4.

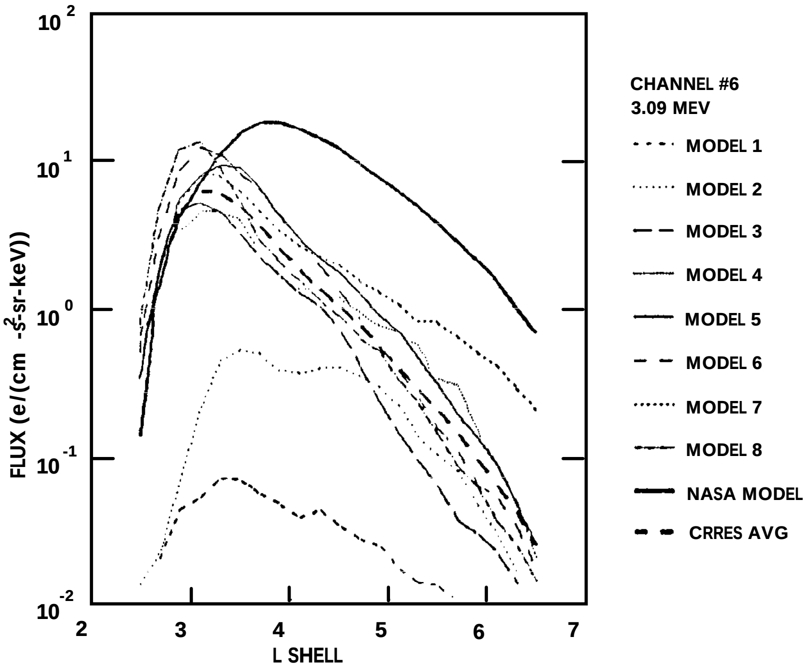

Figure 27 — Computed average radiation belt profiles as functions of *L* (between 2.4 and 6.6) for *E* > 3.09 MeV and for 8 A_{P15} intervals between 5 nT and 55 nT.
(Copyright by and used by permission of Institute of Electrical and Electronics Engineers)

In addition to the DoD efforts, the European Space Agency funded a study aimed at updating AE8 using the CRRES data.[37,38] In this study, the CRRES data were used to train neural networks to predict energetic electron fluxes using the magnetic index K_p as the input. The trained networks then operated on six solar cycles of data (1932–1996) to produce daily averages of fluxes at five energies from 145 keV to 1.57 MeV and six *L* values from 3.0 to 7.0. The daily averages were then used in a superposed-epoch analysis to update AE8, which is defined in terms of a quadratic in solar-cycle epoch. The new model fluxes agree with the CRRES data (for mission averages) within 10%, with typical errors in prediction of less than one-half-order of magnitude for individual daily average fluxes for various energies and *L* values. This study also produced statistical distributions of fluxes and tables of maximal fluxes.

6.2 Magnetospheric Heavy Ions

The next environment to be considered is the trapped heavy ion population. Low to moderate energy O^+ and He^{++} are typically observed throughout the magnetosphere, but the sources of these particles are not entirely clear. The helium nuclei (mostly alpha particles) are possibly from the solar wind,[39] while the O^+ may be primarily of ionospheric origin. In the case of the solar wind, particles probably enter the magnetosphere and are accelerated by radial diffusion. This process, described by Cornwall,[40] adequately describes the magnetospheric helium ion population.[41,42] However, the bulk of this helium population is at energies too low to penetrate the walls of a spacecraft. C, N, and O ions have all been observed although it was not clear whether the particles were trapped in the magnetosphere (recent evidence supports the claim that at least the bulk of the lower energy O^+ is of ionospheric origin). Models by Adams et al.[43] assume that there are a small flux of helium nuclei and a smaller flux of heavier nuclei in the magnetosphere above 10 MeV/nucleon. There are also reports of long-lasting enhancements of the low energy heavy ion fluxes after large solar flares. As yet, these ions are included in radiation dosage calculations in only very specialized applications although they are of concern for SEU effects.

Recently, Grigorov et al.[44] and Cummings et al.[45] have presented evidence for an energetic (≥15 MeV/nuc) trapped heavy ion component associated with the galactic cosmic ray (GCR) anomalous component. Blake and Friesen[39] suggested that the anomalous cosmic ray (ACR) component particles, which may be only singly ionized initially, can penetrate deeper into the magnetosphere than the normal GCR component, which is typically fully ionized. The particles are then ionized near their geomagnetic cutoff and become trapped. This leads to a special trapped population of oxygen, nitrogen, neon, and other elements that may be the source of the observed heavy ion component. The SAMPEX spacecraft[45] recently (late 1992 and early 1993) observed ≥15 MeV/nuc trapped heavy ions with $Z \geq 2$. The trapped population includes He, N, O, and Ne and is located at L~2.[45] The population was seen to increase in intensity in concert with a similar increase in the ACR component.

The geographic distribution of the oxygen particles detected by SAMPEX (which is in an 82° inclination orbit with an apogee of ~670 km and a perigee of ~520 km) is illustrated in Fig. 28[45]. Three distinct populations of oxygen ions are evident. For latitudes above 60°, there is a mixture of GCR and ACR, which have directly penetrated the magnetic field. Between 50 and 60°, there is a mid-latitude component composed of singly ionized (ACR) oxygen, which has a lower latitude cutoff than that of the more highly ionized GCR oxygen. Below 50°, there is a low energy grouping near and below the estimated cutoff of singly charged oxygen. The high latitude and mid-latitude particle populations are present at all longitudes, as would be expected for particles that are controlled by magnetic rigidity. The third population is concentrated in an ~8000 km long band southeast of the South Atlantic Anomaly. The L shell for these particles corresponds to a trapped population at an $L = 2.04 \pm 0.26$. Blake and Friesen[39] predicted that the trapped ACR oxygen would be located at $L = 2.5$–3.5—near where it has now been observed. Thus, the SAMPEX observations verify that the ACR mechanism predicted by Blake and Friesen is a source of trapped ions N, O, and Ne above 27, 21, and 14 MeV/nuc. Helium ions were also observed, but this population is believed to have been trapped by a mechanism other than that proposed by Blake and Friesen and may have another source.[45]

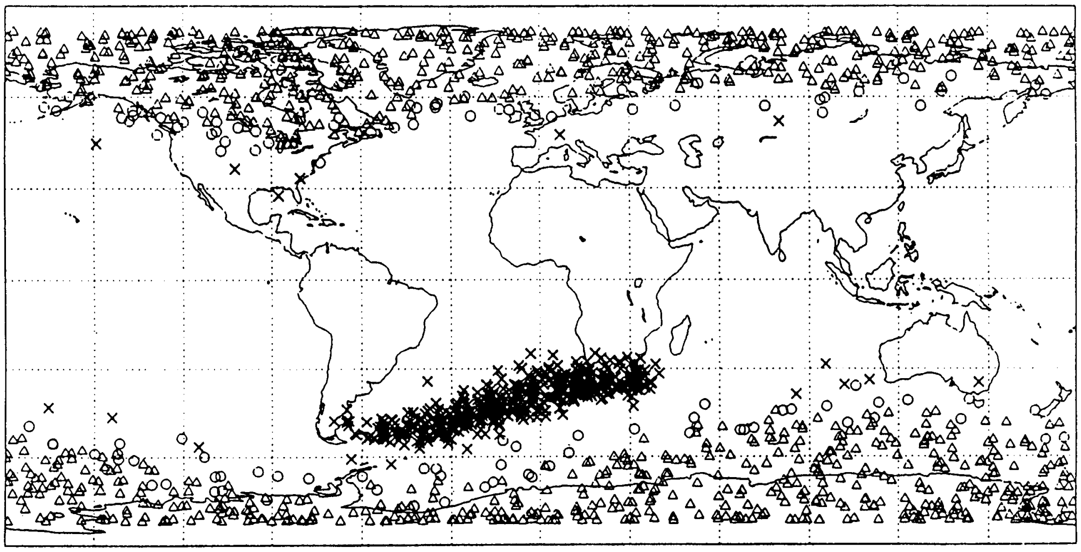

Figure 28 — Geographic distribution of oxygen by SAMPEX between 1992 and 1993. Triangles: events with cutoff energy above vertical O^{+6}, crosses: events with cutoff energy less than O^{+15}, and circles: events with intermediate cutoff energy.
(Copyright by and used by permission of American Geophysical Union)

7. Shielding Design Codes and Optimization

Although it is not an obvious environmental concern, the issue of shielding design and optimization is central to the overall problem of designing and protecting systems from the trapped radiation environment. The characteristics of radiation transport codes—in particular, their requirements for environmental data—need to be carefully considered as part of any comprehensive study of the trapped radiation environment. As in the case of the environment, several radiation shielding codes are currently available: various Monte Carlo simulations, NOVICE (T. Jordan), SHIELDOSE (NASA), the Satellite Assessment Center SatAC Modeling Tool (SMT) developed by the Air Force Research Laboratory, and associated codes like CREME.

Typically these codes (either through Monte Carlo simulations or through approximations to the Monte Carlo results and test data) estimate the effects of individual, high energy charged particles and photons passing through three-dimensional simulations of the spacecraft. Although ground tests have been used to confirm the predictions and in situ data are occasionally reviewed to validate the codes, aside from CRRES, Clementine, and a few activities on the Shuttle, there has been little recent work to systematically validate the codes and to develop new ones. This is an area that needs to be carefully considered in parallel with the development of improved radiation models if a consistent new methodology is to be developed. As was done for CRRES, Clementine, and similar efforts, any long-term study of the effects of the trapped radiation environment must systematically test the existing shielding codes against, first, ground test data and, as it becomes available, the latest in situ data on microelectronics behavior in the radiation environment.

As a matter of common practice, predicted mission environments (behind shielding) should be compared with in situ results and the results distributed. Accurate estimates of the ambient environment and of the actual shielding are prerequisite to properly validate the models. Finally, as TID or SEU rates are the quantities that are actually measured by the spacecraft systems, these quantities, not the ambient particle spectra, are often much more important for engineering studies. Indeed, it makes sense to consider developing a standard dosimeter/SEU detector “flight recorder” much like the black box used on aircraft to monitor these key engineering parameters.

8. Radiation Effects on Advanced Parts

The primary practical reason for interest in the trapped radiation environment is its effects on microelectronics. Microelectronic parts testing, characterization, and selection are potentially among the most expensive and time-consuming processes in spacecraft design—potentially because mission requirements and project procedures can greatly affect the outcome (i.e., a mild radiation environmental requirement might eliminate the problem, while poor design and procurement procedures can lead to severe schedule slip and increased cost late in a program). However, much can be done to control this process.

Current parts procurement procedures need to be reviewed and a systematic procedure developed for enabling the use of commercial parts in space in conjunction with the development of new trapped radiation models. One valuable approach is to compare prelaunch upset rate predictions or dose effects for parts and systems with in situ results; Clementine and several subsequent missions have demonstrated factors as much as 10–100 between on-orbit observations and prelaunch predictions (we currently tend to overestimate radiation effects). Although accomplished on Clementine and increasingly a part of the “faster, better, cheaper” scenario, there is still only a limited attempt to fly “plastic parts” in large quantity in the Earth’s high radiation environment.

Procedures used to procure, test, and characterize such commercial parts need to be based on the details of the radiation environment the spacecraft will encounter. As a facet of this process, ground test procedures and their costs should be reviewed in light of how well they can be used to characterize the in situ effects of radiation. The goal should be to provide direction to the user community on how best to simulate trapped radiation effects on the newer parts types (parts technology is developing much faster currently than our ability to test for radiation effects). As an example, sensitivity to dose rate, particularly low dose rate, has been found to have a pronounced effect on some new families of parts. Thus, any program aimed at developing better trapped radiation models should include an element that not only considers the radiation testing of components and systems but that recommends advanced simulation and testing procedures, particularly for advanced commercial/plastic parts.

9. Shielding Effects and Interactions with Matter

This section briefly reviews how the trapped radiation environment interacts with material. From the standpoint of radiation interactions with matter, three particle families need to be considered:

1) Photons (primarily extreme ultraviolet [EUV], X-ray, and γ-rays).
2) Charged particles (protons, electrons, and heavy ions).
3) Neutrons.

Although numerous, more exotic particles such as positrons, muons, and mesons exist, the above three families account for the vast majority of interactions that concern the spacecraft engineer. In addition, for the impacting particles, mass, charge, and kinetic energy are the principal physical characteristics of interest, whereas mass and density are the key characteristics for the target material. Here, the various types of interactions will be discussed in terms of the first two particle families (neutrons will be ignored because they play no role in the effects of trapped radiation belts on spacecraft systems). The effects of the shielding on these particles will be manifested in terms of energy deposited in a volume (dose) or the energy deposited per unit length in the target material (LET) after traversing a specified thickness of shielding. Thus, the radiation shielding calculation necessary to determine the environment inside a spacecraft breaks down into a three-step process for each particle:

1) Definition of the ambient environment.
2) Propagation of that environment through the shield and calculation of the subsequent changes in the spectrum up to the target.
3) Estimation of the total energy and/or the energy deposition rate at the target.

The first part of this guide detailed the ambient environment. In this section, the latter two issues will be addressed. An important factor that should kept in mind when considering these two issues is the importance of the cascade process to the final result. In this process, one incident particle produces many secondary particles that may be very different from the incident particle (for example, electrons may generate photons or vice versa). These secondaries in turn generate their own secondaries, leading to a complex mix of many different photons and particles. This process repeats until the point of interest is reached or until all initial particle energy is absorbed.

Rather than address this process in its entirety, this section will first discuss the individual, distinct single particle interactions. The final part of this section will describe how, given the characteristics of these individual interactions, Monte Carlo techniques can then be used to estimate the gross effects of the cascade process. In the simplest models, analytic expressions are fit to these results or to actual measurements so that estimates of the end products produced by the cascade are given as a function of depth in the shielding material. The reality is that the cascade process is basically probabilistic and too random to be precisely modeled analytically. However, because analytic fits typically give adequate results in most cases of interest to the engineer, models based on their use will be addressed here for practical radiation shielding calculations.

9.1 Single Particle Interactions

The study of the interactions of a single high energy particle such as a photon or charged particle with matter forms a major subdivision of the physical sciences. Rather than present a detailed quantitative review of each of these interactions, a qualitative description will be presented for each of the main interactions. This will be supplemented with a quantitative plot of the actual interaction when appropriate. The reader is referred to detailed quantitative reviews of each of the processes such as those found in Refs. 1 and 46. In most practical cases, however, the results presented here should suffice for understanding actual computations because the complex equations modeling the processes are normally pre-coded in the computer codes available for conducting shielding calculations.

9.1.1 Photon Interactions

Photons, which propagate at the speed of light and have no charge or rest mass, interact primarily through the photoelectric effect, Compton scattering, and pair production. These interactions all generate free electrons. Consider first the photoelectron process, the probability of which decreases with increasing photon energy and increases with *Z*. In the photoelectron process, the photon is completely absorbed by the emitted (typically) outer shell electron. In one case, however, subsequent interactions are possible—that is, if the photon is energetic enough to emit *K*-shell electrons (inner shell electrons), then this process will dominate ~80% of the time over the emission of outer shell electrons. When an *L* shell (or outer shell) electron subsequently drops down to fill the *K*-shell vacancy, it can emit either an additional X-ray or a low energy Auger electron from the *L* shell (dependent on the *Z* of the material). In Compton scattering, the incident photon is not completely absorbed because the photon is of much greater energy than the atomic electron binding energy. Part of the photon energy goes to scattering the atomic electron (called a Compton electron), and the rest goes into a scattered, lower energy photon. Pair production takes place for photons at energies of 1.02 MeV or higher. A photon of this energy will be completely absorbed by a high-*Z* material. A positron–electron pair will then be formed. Figure 29[47] compares the ranges over which each of the three interactions dominate as functions of *Z* and energy. The solid lines correspond to equal interaction cross sections for the neighboring effects. The dashed line illustrates the situation for photon interactions with silicon. For reference, in silicon, the photoelectron effect dominates at energies <50 keV, pair production at energies >20 MeV, and Compton scattering at intermediate energies. Of course, the products of these interactions (electrons, photons, and positrons) can further interact with the target material, producing a complex cascade of electrons and photons.

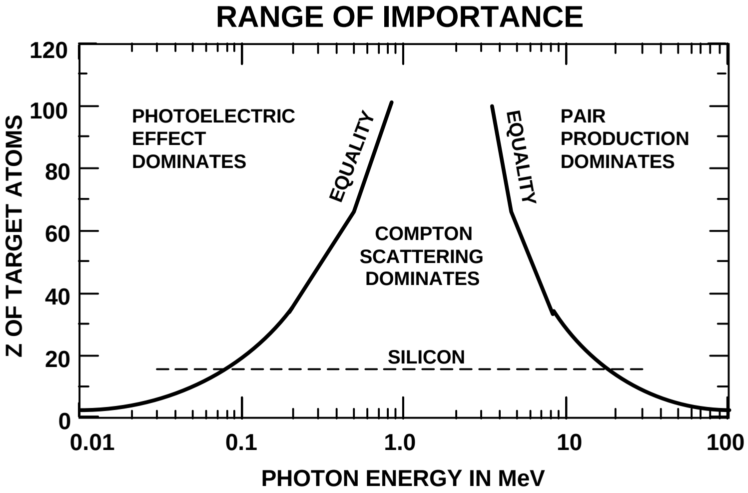

Figure 29 — Three photon interactions as a function of *Z* and photon energy
(Copyright by and used by permission of Institute of Electrical and Electronics Engineers)

9.1.2 Charged Particle Interactions

Charged particles interact with matter primarily in two ways: Rutherford scattering and nuclear interactions. Rutherford (or Coulomb) scattering, in which the charged particle interacts with the electric field of the target atom, typically dominates. It results in both excitation and ionization of atomic electrons and, for sufficiently energetic impacts, can transfer enough energy to displace atoms within the lattice structure. As an example, for electrons, a minimum energy of ~150 KeV is required to cause displacement in silicon, while only 100 eV is required for protons. Nuclear interactions, where the impacting particle actually interacts with the atomic nucleus, can result in elastic or inelastic scattering and transmutation (through fusion or fission). As an example, a nucleus can absorb a proton and emit an alpha particle. This process, called spallation, and the recoil atoms that result from displacement can transform a relatively benign proton environment into an SEU-causing heavy ion environment because the heavy ions have much larger LETs compared with the protons. Also, long-term exposure to the space radiation environment, through transmutation, may make the spacecraft material itself radioactive.

One quantitative measure of the interaction of a high energy particle with matter is stopping power or energy loss per unit length in a given material. As an example, low energy electrons (~10 keV) primarily cause ionization. The amount of energy deposited by the latter and protons in producing ionization can be determined from stopping power tables (electrons: Berger and Seltzer[48]; protons: Janni[49,50]). Stopping power is essential in calculating the Heinrich flux necessary for most SEU calculations. Stopping power (or, approximately, LET) in terms of MeV·cm^2/g is given in Fig. 30 for electrons, protons, and various heavy ions in silicon.[3]

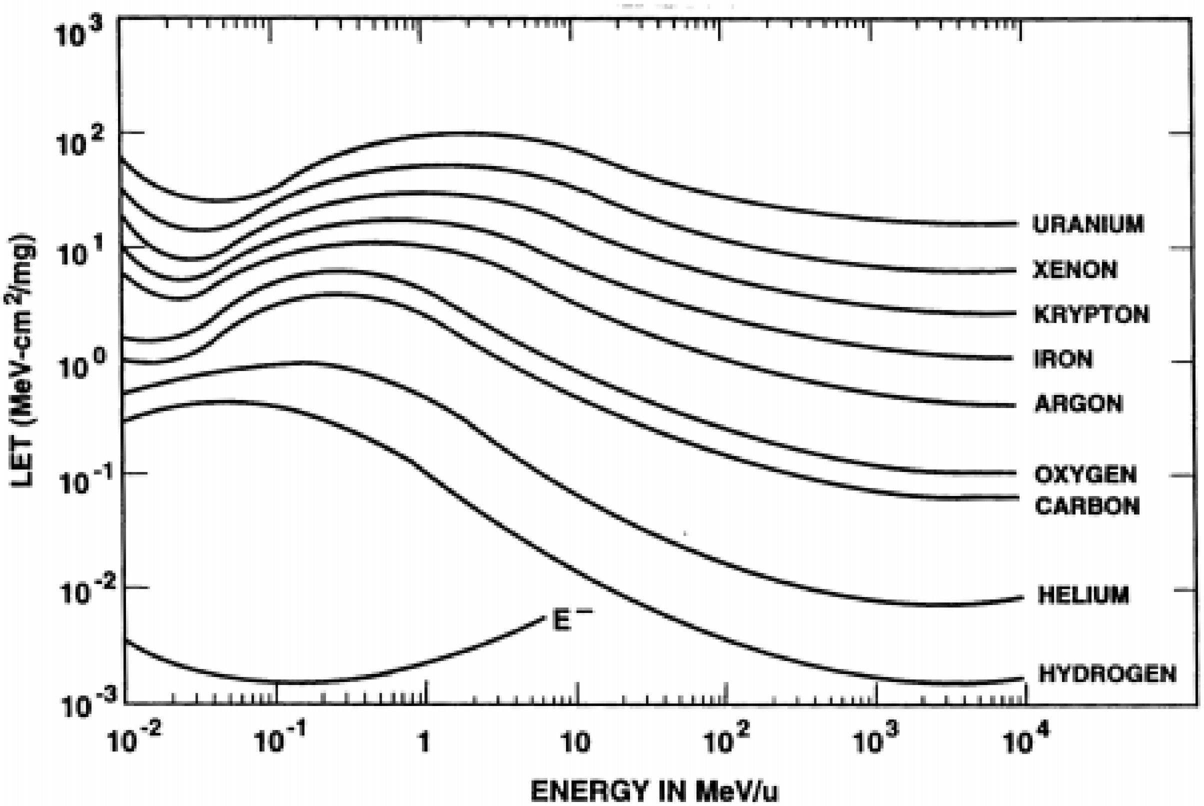

Figure 30 — The stopping power (or LET) vs energy per atomic mass unit for a variety of ions and electrons in silicon

A second quantitative measure of high energy particle interactions closely related to stopping power is the penetration depth/range or the maximum distance a particle of a given energy can penetrate. This depth can be used to roughly estimate the minimum cutoff energy for a given thickness of spacecraft shielding and hence its effectiveness. Figure 31 compares the penetration depth of electrons and protons in aluminum for different energies (the range of heavier ions in Al are presented later in Fig. 36). In particular, note that an electron at 1 MeV penetrates more than 100 times more shielding (~0.2 cm) than a 1 MeV proton (~0.0015 cm). Similarly, it takes a ~20 MeV proton to penetrate to the same depth as a 1 MeV electron. Because ~0.1–0.2 cm (40–80 mil) is a typical shielding level, it is common to compare the integral dose for E ≥ 1 MeV electrons with E ≥ 20 MeV protons because these are the primary contributors to the radiation environment behind the spacecraft shield.

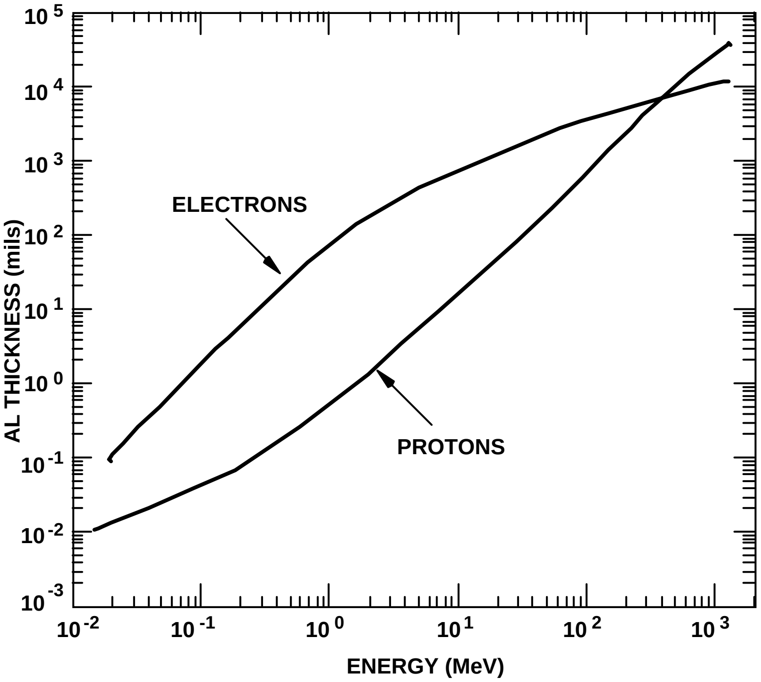

Figure 31 — Minimum penetration energy for electrons and protons vs shield thickness

9.2 Modeling the Effects of Shielding

If the detailed evolution of a particle passing through matter is followed, the interaction of the particle with shielding becomes increasingly complex as each interaction gives rise to a cascade of byproducts. Fortunately, as each interaction disperses the energy into more byproducts, a point is reached when the byproducts and the original incident particle (if it still exists) no longer have sufficient energy to excite further interactions—the process has a finite conclusion. Although it is common practice to use Monte Carlo techniques to model the detailed passage of a particle through shielding, the computer codes that accomplish this can require super computers or take many hours to perform the calculations. As a consequence, it is common to run the detailed codes for a range of variables, and then use this information to derive analytic fits for the end products of the multiple interactions that are created following the original particle impact. The effects of these byproducts are then approximated roughly in terms of displacement damage, energy deposition, or ionization (or electron–hole creation). Normally, these algorithms, not the detailed computations, are used to actually model radiation effects.

As a specific example of the Monte Carlo results, consider electrons. Electrons are particularly easily scattered in a material. Rather than passing through the material, they and the secondary electrons they generate are scattered into the material. This behavior is illustrated in Fig. 32, which is a computer simulation (Monte Carlo) of the trajectories of electrons impacting on a copper target.[51,52] Note that many of the electrons are actually scattered back out of the surface of the material. This behavior becomes ever more complex as the thickness of the shield decreases as illustrated in the figure.[51,52] It is readily apparent in these Monte Carlo simulations that the dose is very dependent on the shape (or thickness) of the shield. This scattering of the electrons and their byproducts by the shielding means that the details of geometry of the shielding must be considered in any radiation calculations.

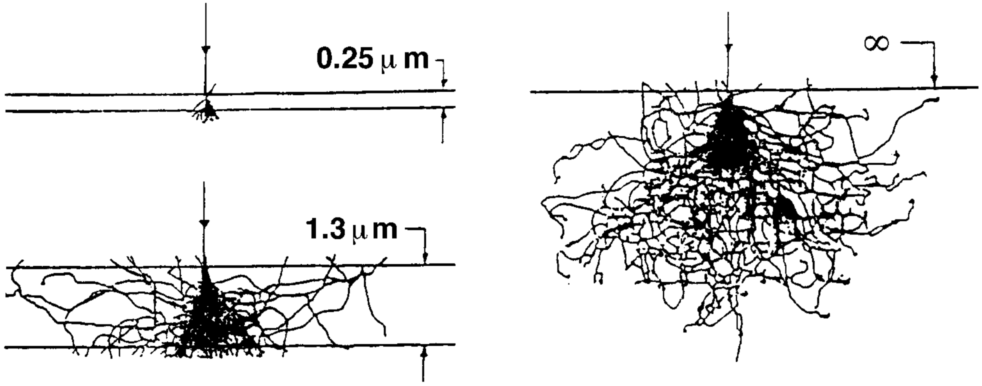

Figure 32 — Monte Carlo results showing the effect of varying target thickness
(Copyright by and used by permission of Institute of Electrical and Electronics Engineers)

Analytic expressions (as an example of this for electrons, see Ref. 53) have been fit to the results of Monte Carlo calculations (Fig. 32) and to actual measurements for electrons, protons, heavy ions, neutrons, and photons. Specific characteristics, such as energy deposition, ionization, flux (both forward and back-scattered), and dose, can then be predicted as functions of shielding thickness or material. Figure 33 illustrates this effect for one characteristic—the electron dose vs distance into the shielding material as the incident electron energy is increased. Here the region over which the electron deposits it energy is smeared out along its track. Compare this with Fig. 34 for a proton—a high energy ion deposits its energy primarily near the end of its track. This difference in energy deposition with shielding thickness is often used in designing solid-state particle detectors capable of discriminating between high energy electrons and protons. It also must be kept in mind when designing shielding because too much shielding can actually cause cosmic rays of a particular energy to deposit most of that energy at a specific point in a device rather than passing through it. Families of similar parametric curves have been developed to allow rapid calculations of the effects of shielding (however, the lengthy Monte Carlo calculations are often retained in detailed shielding studies).

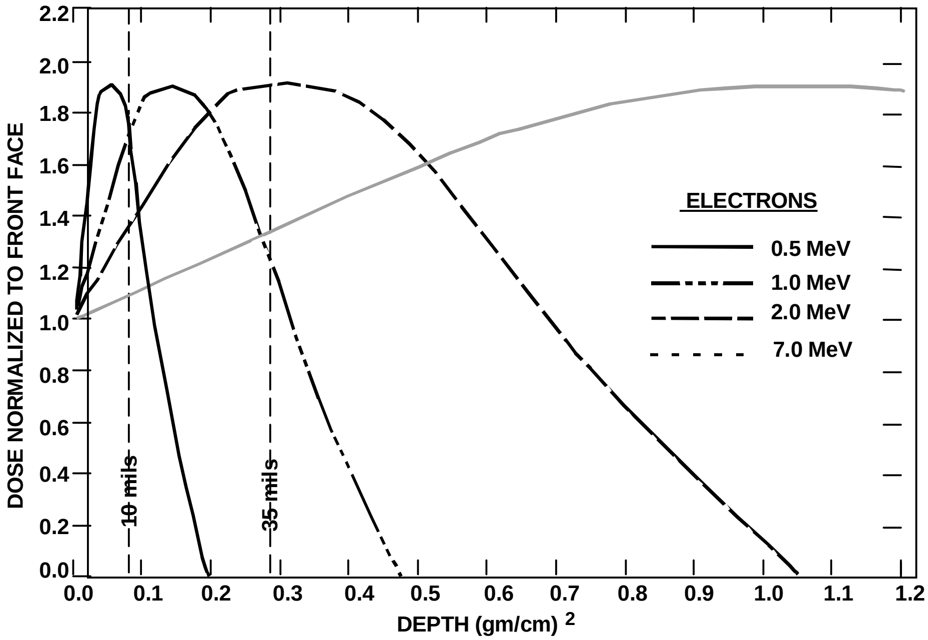

Figure 33 — Electron dose as a function of depth for CAFMn TLDs. The dosage is normalized to 1 at the front face.

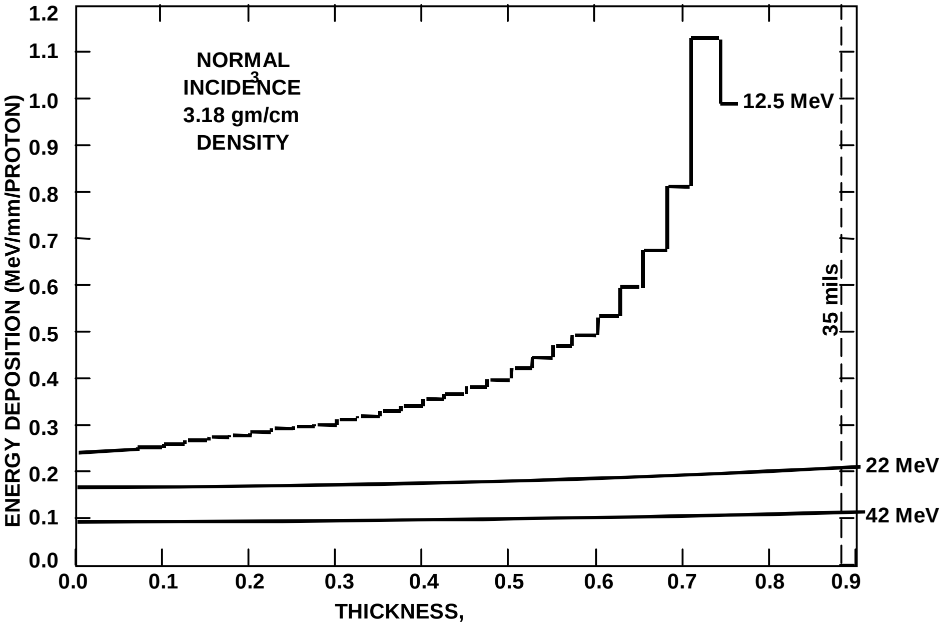

Figure 34 — Proton energy deposition as a function of depth for CaF_2

These considerations allow a simple description of how the radiation dose environment is determined inside a spacecraft. If the interaction is limited to dosage, then the following, very simple one-dimensional model describes the basic mathematical steps involved:

For dose, assume a target of density ρ, area δA, and thickness $\delta\tau = M/\rho\delta A$:

1) Determine the attenuation effects of the shielding on the ambient flux spectrum of the particles of interest.

2) Compute the attenuated flux (number *N* of particles per unit area δA normal to the surface) vs energy at the target surface. Call this *f*(*E*) at energy *E* such that:

$$f(E) = \frac{N(E)}{\delta A} \tag{28}$$

3) Estimate (i.e., from Fig. 33) the change in energy δE in crossing the target thickness $\delta\tau$ at the appropriate distance in the shield for a particle of initial energy *E*:

$$\delta E \approx \delta\tau \frac{\mathrm{d}E}{\mathrm{d}x}\bigg|_E \tag{29}$$

4) The dose per particle of energy *E* is approximated by:

$$D(E) \approx \frac{\partial E}{M} \approx \frac{\mathrm{d}E}{\mathrm{d}x}\bigg|_E \frac{\delta\tau}{M} \approx \frac{1}{\rho}\frac{\mathrm{d}E}{\mathrm{d}x}\bigg|_E \frac{1}{\delta A} \tag{30}$$

5) The total dose at energy *E* is:

$$D_T(E) \approx ND(E) \approx \frac{1}{\rho}\frac{\mathrm{d}E}{\mathrm{d}x}\Big|_E f(E) \qquad (31)$$

6) The total dose for $E \geq E_0$ is then given by integrating Eq. (31) over the range E_0 to ∞.

This process, repeated for many different angles and particles, gives the total dose inside a three-dimensional volume. The final answer is basically independent of the shape or size of the test point and is only a function of the density of the material.

In actual dosage calculations, because of the various effects of shielding on the energy deposition, five shielding geometries are typically considered (Fig. 35). These five geometries (as adapted from the descriptions provided by T. Jordan for his NOVICE shielding code[54]) are as follows:

1) Spherical shell. As the name implies, this configuration represents a hollow sphere of equal thickness in every direction from the dose site, which is at the center of the sphere (note: the radius of the sphere void can be shown to be unimportant for large distances). The dosage tends to be lower than that for a solid sphere of the same shield thickness. This case resembles a point inside a typical hollow spacecraft.

2) Sphere. The shield is assumed to be uniformly distributed around the dose site with no gap between the shielding material and the dose site (i.e., a point at the center of a solid metal sphere). As scattering takes place relatively close to the dose site, little scattered flux is lost. This case resembles a spot shield configuration.

3) Slab (or 2*Slab). A single slab is assumed to be an infinite two-dimensional surface. Ideally, particles enter from one side and irradiate the dose site. That is the basic single slab configuration that assumes no back scattering of electrons and no flux from behind (i.e., infinite back shield); this approximates the actual case for high energy protons and heavy ions. Typically, to estimate the omnidirectional flux for a part between two shield planes without back scattering from a second surface, double this value (in the NOVICE code, this is called the 2*Slab case; see double slab case also).

4) Back slab. This configuration is similar to the slab in that the dose site is again assumed to be backed up by an infinite slab. As before, the flux only comes in from one side, but now particles can be reflected or scattered back. This often nearly doubles the incident flux for electrons.

5) Double slab. Here there are two identical thin shields—one on each side. In this configuration, the flux is assumed to come from both sides, and back scattering from each is included. This geometry would resemble the case of a flat solar array panel extending from the spacecraft in a wing configuration.

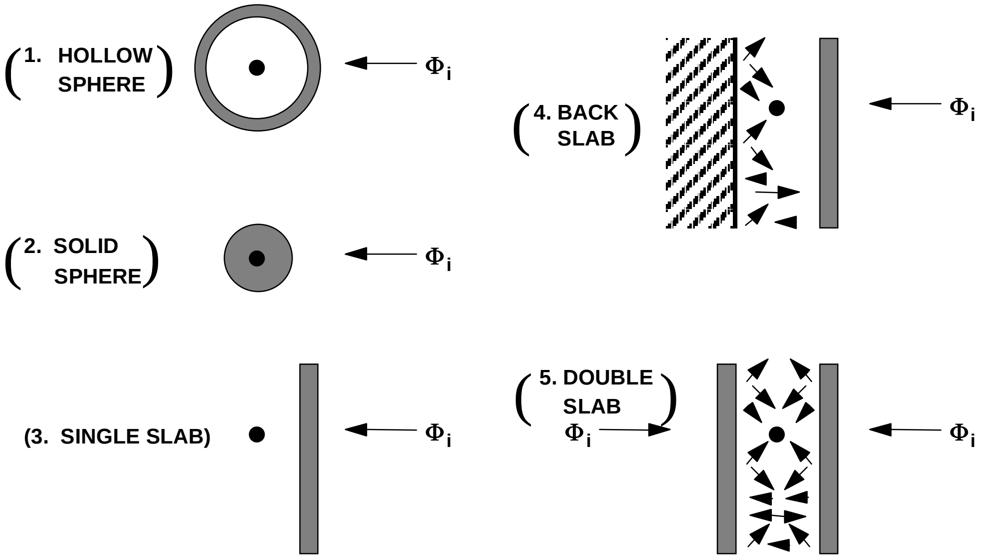

Figure 35 — Five shielding configurations considered in the NOVICE code for calculating dosage. Note that examples 3 and 4 are doubled by the code.

Which configuration to use depends greatly on the geometry of the spacecraft component being modeled. The spherical shell is often used as the baseline representation because it more closely resembles the shielding around typical circuit boards in the spacecraft interior.

Consider next the detailed steps involved in determining the other radiation quantity of interest, the Heinrich curve for a heavy ion. As outlined in Adams et al.[5] for the CREME code, the steps are as follows:

1) Define the particle spectrum of interest at the surface of the critical volume. In this example, consider the ambient environment for GCR iron at the surface of a spacecraft. Figure 2 is a plot of the ambient GCR iron flux as a function of energy for three cases: 90% worst case, solar minimum, and solar maximum. Call this differential spectrum $f(E)$.

2) The attenuation of a high energy ion by shielding can be approximated by the following (spallation is ignored[5]):

$$f'(E') = f(E)\left[\frac{S(E)}{S(E')}\right]e^{-\sigma\tau} \qquad (32)$$

where

$$\sigma = \frac{5\times10^{-26}\eta\left(A^{1/3}+27^{1/3}-0.4\right)^2}{27} \qquad (33)$$

f' = differential spectrum inside shielding
τ = thickness of shielding
E' = energy inside spacecraft = $R^{-1}\{R(E)-\tau\}$
R = range through shield of ion of energy E (see Fig. 36 for Fe in Al)
R^{-1} = inverse function of $R(E)$
S = stopping power of ion in target material (see Fig. 30 for Fe in Si)
A = atomic mass of ion
η = Avogadro's number

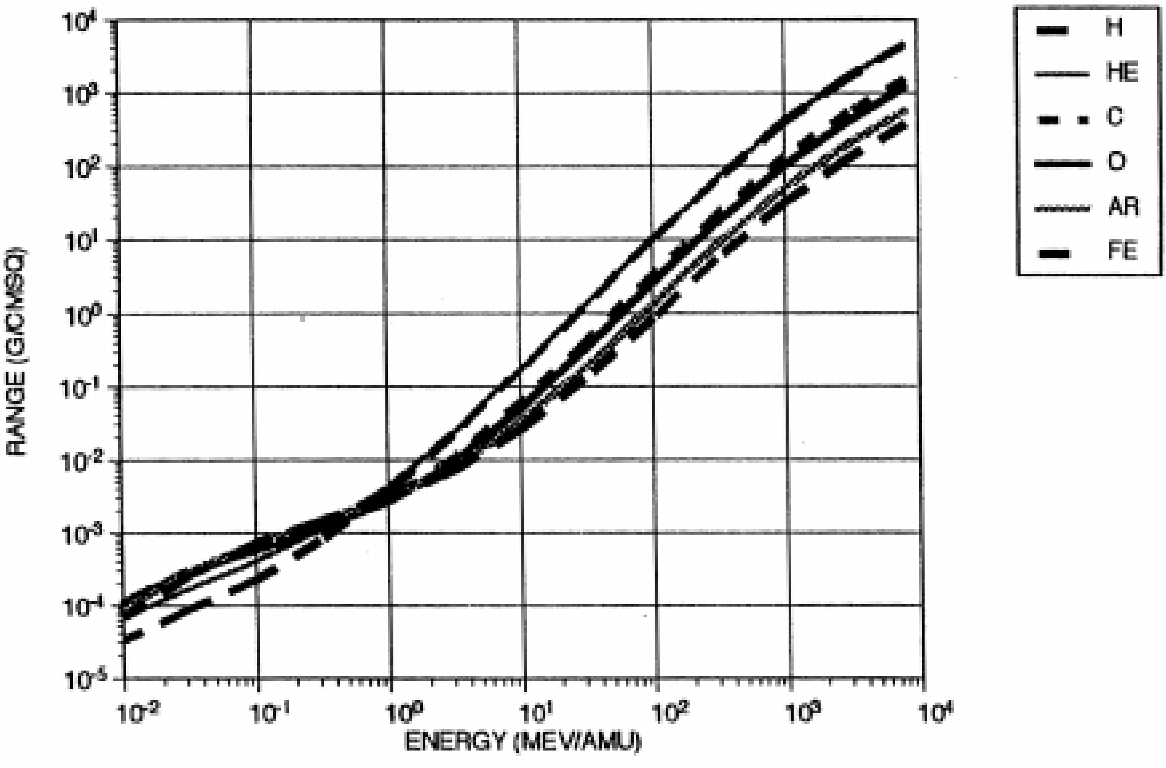

Figure 36 — Ion range vs energy in Al for H, He, C, O, Ar, and Fe.

Figure 37 shows the results of this calculation for Fe behind 25 mil of Al shielding.[5]

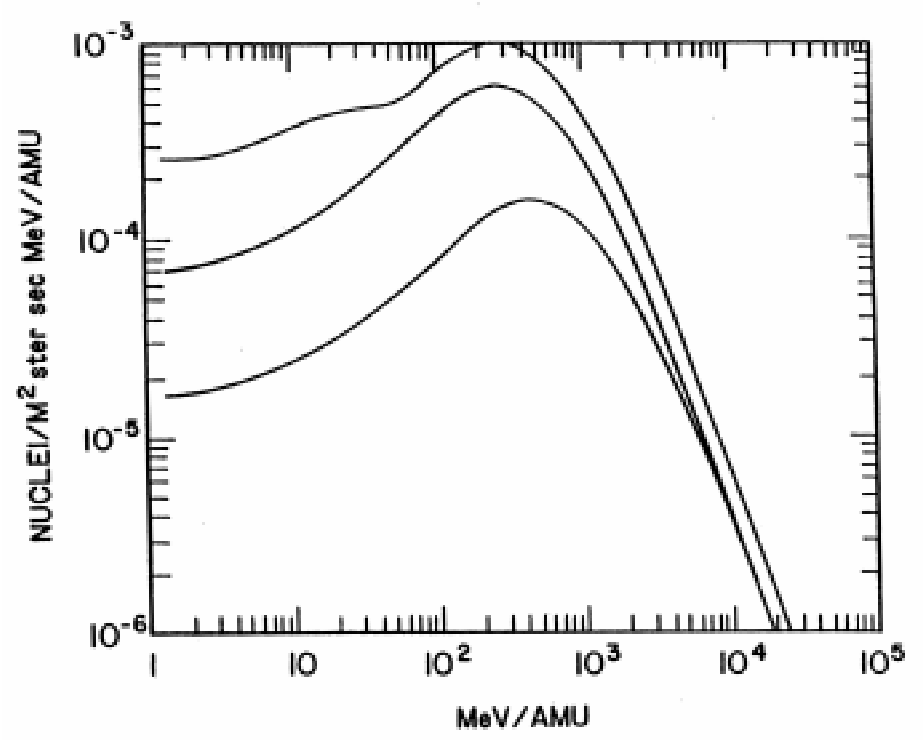

Figure 37 — Shielding attenuated cosmic ray differential iron spectra for the three cases in Fig. 2

3) The d*E*/d*x* vs energy curve for the incident particle species in the material of interest is determined. The d*E*/d*x* curve for Fe in Si is plotted in Fig. 30. Set $LET = \frac{1}{\rho}\frac{\mathrm{d}E}{\mathrm{d}x}$. This curve relates LET to particle energy *E*'.

4) The incident (internal) differential particle spectrum *f*'(*E*') is converted to the differential Heinrich spectrum *h*(*L*) by:

$$h(LET) = f'(E')\frac{\mathrm{d}E'}{\mathrm{d}LET} \tag{34}$$

(Note: A given LET may correspond to several values of *E*', c.f. Fig. 30)
This result for Fe impacting Si is presented in Fig. 38 (the spikes at the ends of the curve are numeric and result from d*LET*/d*E* going to 0, which implies that d*E*/d*LET* goes to ∞; a careful analytic evaluation would give a finite value).

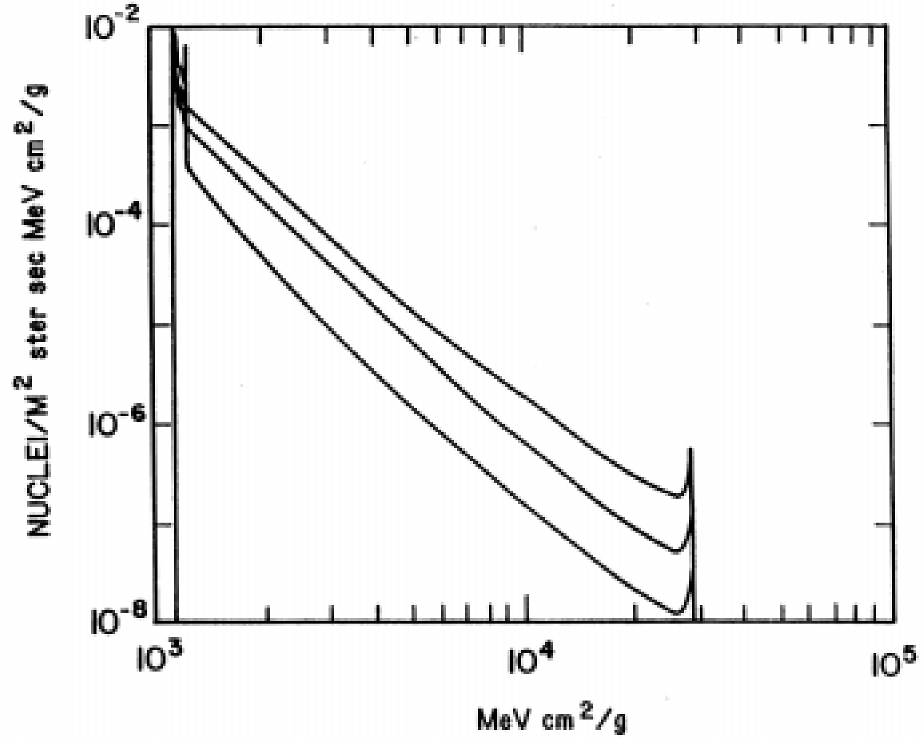

Figure 38 — The same three cases as in Fig. 2, but now the spectra have been transformed into differential LET spectra

5) Equation (34) is integrated over LET to give the integral Heinrich LET curve, F_H [note: this is equivalent to Eq. (7)]:

$$F_H(LET) = \int_{LET}^{\infty} h(l)\mathrm{d}l \tag{35}$$

The final results are plotted in Fig. 5. These curves, called Heinrich curves, are the type of information normally required for SEU calculations. In the case of GCR, this curve would be calculated for all GCR and summed to give a final result. The SEU rate dU/dt is determined by integrating the product of the three-dimensional SEU cross section σ and the Heinrich curve over angle and LET, and then summing over particle species.

To summarize, there are many different techniques for estimating the radiation environment behind a spacecraft shield. To limit the amount of computer time required, the exact Monte Carlo formalism is often replaced by analytic approximations (called kernels) when performing the particle transport and shielding calculations. Specifically, tabulated attenuation data, using Monte Carlo techniques, are prepared for various shield geometries (e.g., the slab, spherical shell, and solid sphere geometries illustrated in Fig. 35). Given a three-dimensional model of the shielding mass and geometry (or a one-dimensional configuration, depending on the desired level of accuracy), the equivalent shielding at a point as a function of angle and path length is calculated. The input spectra from the environment (neutrons, γ-rays, photons, electrons, positrons, protons, heavy ions, alphas, GCR) are convolved with this equivalent shielding to calculate the dose (or Heinrich flux) as a function of energy (or LET) and angle. Secondary and bremsstrahlung particle effects also normally need to be included, particularly for thick shielding. For a more detailed treatment of these interactions see Refs. 1, 46, and 55–57. (Computer codes for carrying out detailed transport and shielding calculations are available from the Oak Ridge National Laboratory's Radiation Shielding Information Center [RSIC] and various commercial vendors and government laboratories. The RSIC address is ORNL, Box X, Oak Ridge, TN 37831-6362, Telephone 423-574-6176.)

10. Radiation Environment Estimates

In this section, the review of the trapped radiation environment is completed by combining estimates of the ambient radiation environment with the transport/shielding process to provide a practical case study. A detailed analysis of the radiation dose environment to be expected for a lunar transfer mission is used to illustrate the basic steps required in implementing a thorough analysis of the radiation environment inside a spacecraft.

To illustrate the process of estimating the radiation dose environment within a satellite, consider the case of the Clementine spacecraft lunar transfer orbit sequence. Clementine was an ambitious DoD/NASA mission designed to map the moon and an Earth orbit-crossing asteroid. It was the first mission the United States flew to the moon in more than 20 years, and it tested the effects of the radiation environment on a number of unique, advanced microelectronic systems. The Clementine spacecraft left behind its lunar transfer stage in a unique, highly elliptical orbit that passed repeatedly through the trapped radiation belts. This interstage and Clementine were both instrumented with radiation dosage and SEU detectors. In addition, they carried boxes of advanced microelectronics components for direct exposure to the radiation environment. A detailed radiation environment prediction was required to allow the identification of radiation sensitive parts and to determine appropriate replacement parts or provide enhanced protective measures. It was also desired to predict the performance of the systems and test components in the radiation environment. These are all typical requirements for a space mission and illustrate the wide range of potential requirements that a trapped radiation model might be expected to address.

Consider the trapped radiation environment anticipated by Clementine. This environment was estimated using the AE8 (electron) and AP8 (proton) solar maximum (or active) and solar minimum (or quiet) trapped radiation models. These models give dosage results that, when averaged over mission lifetimes of the order of the solar cycle, are typically within a factor of 2 of the actual measured dosages. As discussed earlier, for time periods shorter than approximately five years, the statistical variations can be great (approaching factors of $10^{\pm 1}$ to $10^{\pm 2}$ for missions of less than one year, Fig. 16). Even so, with a properly defined radiation design margin (RDM), the predictions are useful for evaluating a spacecraft radiation hardness design. In the case of Clementine, the project used a conservative RDM of 4 (e.g., estimated dose values were multiplied by 4 to provide a worst case design requirement for parts) for design purposes.

As has been described, the process of calculating the dosage at the interior of a spacecraft is straightforward but time consuming. In the case of Clementine, the *B* and *L* coordinates of the spacecraft were estimated from the orbit. The particle integral flux as a function of energy was then computed in terms of *B* and *L* from the AE8/AP8 models. The resulting spectra were summed over mission time to give the total integral fluence spectrum in terms of energy and particle species. These spectra, by species, were then used as input to the shielding code (T. Jordan's NOVICE code, a commercially available software package, was used for the Clementine estimates[56]), which computes the total energy deposited at a point as a function of shield thickness, shield composition, and geometry. Typically, for dosage calculations to be used in a first-order estimate of the internal radiation environment, the composition is assumed to be aluminum for the shield and silicon for the dose site. Geometrical considerations become particularly important for electrons as the electrons can be easily scattered or reflected within the material. As described in preceding sections, several different geometries are usually assumed. Here, five geometries were considered (see Fig. 35):

1) Spherical shell.
2) Sphere.
3) 2*slab.
4) Back slab.
5) Dubl slab (double slab).

In the NOVICE calculations, the single slab is assumed to be an infinite two-dimensional surface (Fig. 35) with an infinite back shield; no radiation comes from behind the shield, and none is reflected back. For comparison purposes, the code doubles this value (hence, 2*slab) so that the results can be used to estimate the omnidirectional flux for a part between two slabs without scattering (see dubl slab case). Unless stated otherwise, the spherical shell geometry is assumed as the baseline representation because it more closely resembles the shielding around typical circuit boards in the Clementine interior.

A set of orbital data for the portions of the Clementine orbit within 11 Earth radii was assembled (note: the Clementine orbit, as is true for most missions, underwent continual revision; the calculations here represent only one of several options considered). The Clementine orbit was divided into six segments. These were:

1) 1994/01/24 (01:48)—1994/01/26 (01:00) (initial parking orbit).
2) 1994/01/26 (01:00)—1994/01/30 (06:44) (Earth–moon transfer injection).
3) 1994/01/30 (07:00)—1994/02/09 (12:00) (Earth–moon transfer orbit).
4) 1994/02/09 (12:00)—1994/02/21 (01:09) (Earth–moon transfer orbit).
5) 1994/05/03 (13:17)—1994/05/15 (12:00) (Earth gravity-assist flyby).
6) 1994/05/15 (12:00)—1994/05/27 (18:08) (Earth gravity-assist flyby).

For these orbits, the dosage for the five geometric configurations, solar maximum and solar minimum environmental assumptions, and various shielding thicknesses were calculated to provide an estimate of the range of doses to be expected. Radiation doses for electrons, protons, and photons (secondary particles) were calculated for all segments when Clementine would be inside ~11 R_E (the AE8 models are only useful inside ~11 R_E and the AP8 models within ~6 R_E).

The results in terms of dosage are presented in Figs. 39 and 40 for two worst case orbital segments—the trapped electrons at solar maximum and protons at solar minimum and the first transfer orbit—and are tabulated in Table 2 for 58 mil of aluminum shielding. Note the wide variation in results for the electrons; as has been discussed, the precise geometric assumptions can make a big difference in results. The main difference between the proton results occurs between the two- and three-dimensional geometric assumptions—plane vs sphere.

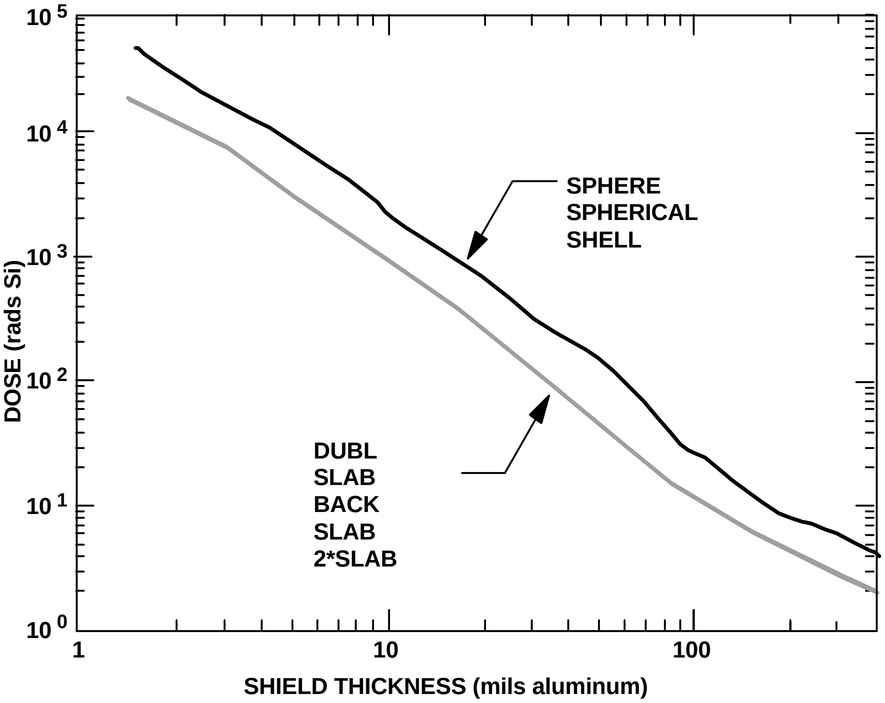

Figure 39 — Radiation dosage from the trapped proton environment (AP8) for solar-quiet conditions and for the first Earth-moon transfer orbit

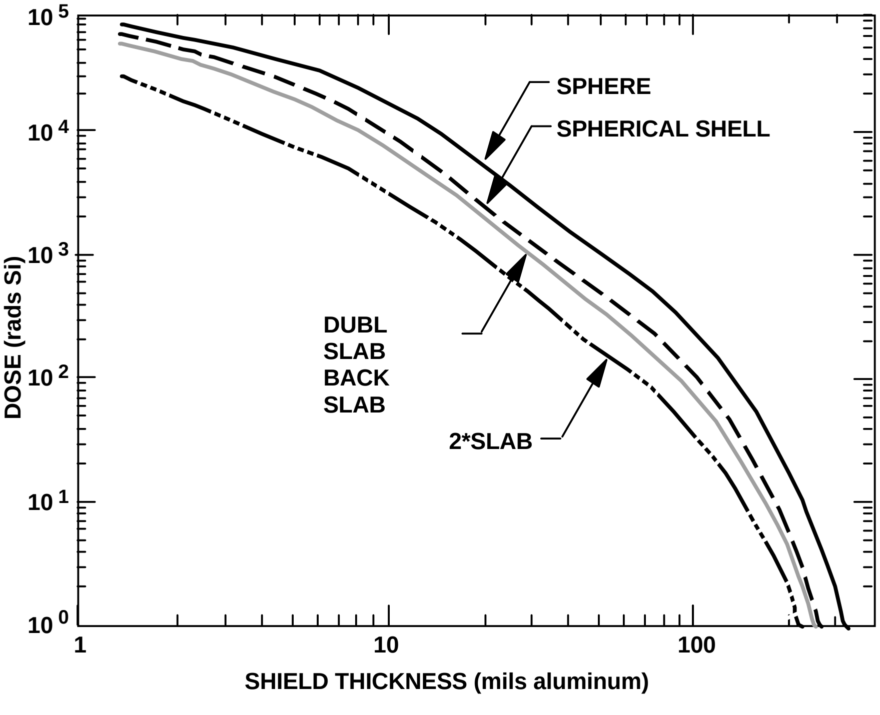

Figure 40 — Radiation dosage from the trapped proton environment (AP8) for solar-active conditions and for the first Earth-moon transfer orbit

In many cases, the spherical shell geometry is the most appropriate because it resembles the structure of a spacecraft surrounding circuit boards in the interior of the spacecraft. Spherical shell results for the Clementine interstage mission are summarized in Fig. 41 (the interstage had a perigee of ~500 km, an apogee of ~160,000 km, and an inclination of 67°). Note that the proton dose due to trapped radiation is very low in comparison to the trapped electrons for the interstage. To conclude, Figs. 39–41 were used in the design of the Clementine mission (with an additional RDM of 4) and represented the type of design information usually provided to a project.

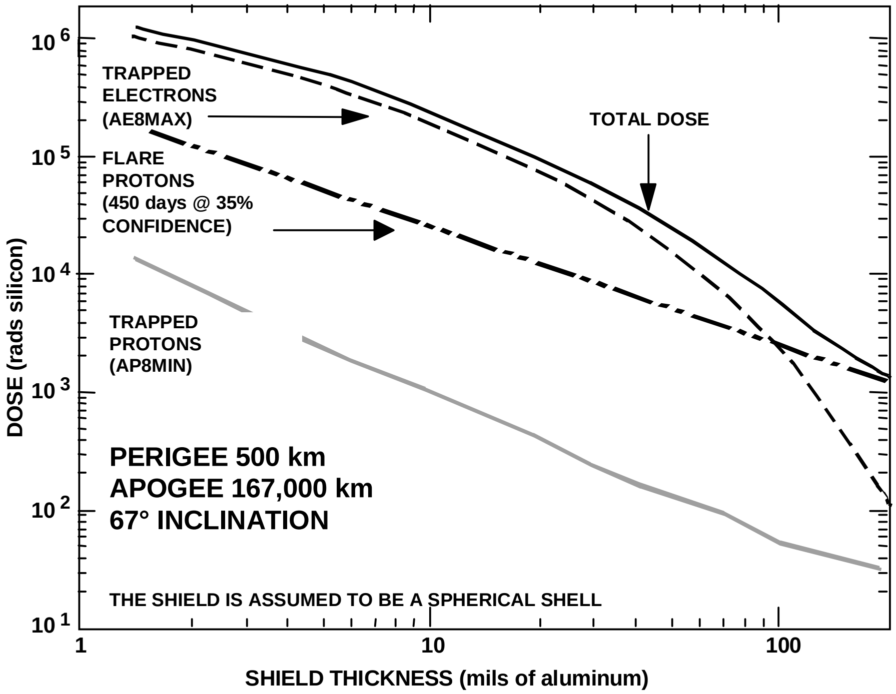

Figure 41 — Mission summary plot for the total radiation dose expected for the Clementine interstage. This assumes a 450-day mission and a 95% confidence flare environment.

TABLE 2. Summary table for dosage behind 58 mil shielding for the trapped electron (AE8) and trapped proton (AP8) environments. Results correspond to differing levels of geomagnetic activity, geometry, and orbit. Units are rads(Si).

Clementine TRAPPED RADIATION ENVIRONMENT ESTIMATES

Active Electrons		58 Mil		DOSAGE (Rads)			
	Orbit Phase	Date	SPHERE	SPH SHELL	2*SLAB	DUBL SLAB	BACK SLAB
1.	Low Earth Orbit	94/01/24	0.001150	0.000437	0.000154	0.000315	0.000315
2.	Earth-Moon Trans	94/01/26	184.000	83.500	32.600	61.300	61.400
3.	Earth-Moon Orbit	94/02/04	778.000	359.000	127.000	260.000	260.000
4.	Earth-Moon Orbit	94/02/15	466.000	201.000	78.400	143.000	143.000
5.	Earth Grav Assist	94/05/06	247.000	88.400	30.100	60.400	60.400
6.	Earth Grav Assist	94/05/24	665.000	267.000	107.000	183.000	183.000
	TOTAL DOSE		2340.001	998.900	375.100	707.700	707.800

Active Protons		58 Mil		DOSAGE (Rads)			
	Orbit Phase	Date	SPHERE	SPH SHELL	2*SLAB	DUBL SLAB	BACK SLAB
1.	Low Earth Orbit	94/01/24	0.001800	0.001800	0.001310	0.001310	0.001310
2.	Earth-Moon Trans	94/01/26	29.000	29.000	9.780	9.780	9.780
3.	Earth-Moon Orbit	94/02/04	104.000	104.000	31.900	31.900	31.900
4.	Earth-Moon Orbit	94/02/15	66.800	66.800	19.400	19.400	19.400
5.	Earth Grav Assist	94/05/06	0.000	0.000	0.000	0.000	0.000
6.	Earth Grav Assist	94/05/24	0.000	0.000	0.000	0.000	0.000
	TOTAL DOSE		199.802	199.802	61.081	61.081	61.081

Quiet Electrons		58 Mil		DOSAGE (Rads)			
	Orbit Phase	Date	SPHERE	SPH SHELL	2*SLAB	DUBL SLAB	BACK SLAB
1.	Low Earth Orbit	94/01/24	0.001120	0.000434	0.000153	0.000312	0.000312
2.	Earth-Moon Trans	94/01/26	128.000	56.300	21.700	41.400	41.400
3.	Earth-Moon Orbit	94/02/04	557.000	250.000	87.500	181.000	181.000
4.	Earth-Moon Orbit	94/02/15	466.000	201.000	78.400	143.000	143.000
5.	Earth Grav Assist	94/05/06	247.000	88.400	30.100	60.400	60.400
6.	Earth Grav Assist	94/05/24	665.000	268.000	107.000	183.000	184.000
	TOTAL DOSE		2063.001	863.700	324.700	608.800	609.800

Quiet Protons		58 Mil		DOSAGE (Rads)			
	Orbit Phase	Date	SPHERE	SPH SHELL	2*SLAB	DUBL SLAB	BACK SLAB
1.	Low Earth Orbit	94/01/24	0.001800	0.001800	0.001310	0.001310	0.001310
2.	Earth-Moon Trans	94/01/26	29.100	29.100	9.830	9.830	9.830
3.	Earth-Moon Orbit	94/02/04	104.000	104.000	32.000	32.000	32.000
4.	Earth-Moon Orbit	94/02/15	66.700	66.700	19.400	19.400	19.400
5.	Earth Grav Assist	94/05/06	0.000	0.000	0.000	0.000	0.000
6.	Earth Grav Assist	94/05/24	0.000	0.000	0.000	0.000	0.000
	TOTAL DOSE		199.802	199.802	61.231	61.231	61.231

		DOSAGE (Rads)		58 Mil	
	SPHERE	SPH SHELL	2*SLAB	DUBL SLAB	BACK SLAB
TOTAL ACTIVE DOSE	2539.80	1198.70	436.18	768.78	768.88
TOTAL QUIET DOSE	2262.80	1063.50	385.93	670.03	671.03

11. Recommendations

The preceding discussion indicates several areas that need to be addressed in updating and evaluating the current trapped radiation environment tools. In a departure from conventional approaches, it has been suggested that an effort should be made to understand the needs of the user community—shielding designers and electronic parts engineers. Not just the trapped radiation models, but the transport codes and the radiation effects models, need to be considered in any update. The rapid movement to commercial parts and systems is particularly crucial to the future of radiation modeling and must be factored into the design of the next generation of trapped radiation environment tools (in contrast to older models). Emphasis must also be shifted to determining how well the tools predict the effects of the radiation environment; a model capable of predicting precisely one facet of the trapped radiation environment does no good if that facet has little bearing on the environmental effect to be modeled. As an example, angular distributions, composition, and time-dependent variations need to be more carefully addressed than in the past because these factors may be more important than simple average dose estimates in designing optimal radiation shields for a constellation of ~100 spacecraft. Although not discussed, the time-dependent characteristics of new phenomena such as low dose rate effects and internal charging also need to be factored into any future modeling efforts. (Low dose effects depend on low doses for long periods of time, while internal charging effects can respond to changes in the electron flux of only a few hours.)

In summary, the following is recommended:

1) As they stand, the trapped radiation environment tools need to be updated with the latest particle and magnetic field data available. Given the Internet and current computing resources, this could become a real-time activity; as new data becomes available, the “master” tool set is updated automatically. An international standard reference radiation model needs to be developed (particularly in the light of the movement to ISO standards).

2) Short-term variations, time dependence, angular variations, and composition need to be included in any future standard model, with provisions for the long-term variations of these properties.

3) Single event effects (SEEs) and the requirement to predict radiation effects on the overall system response need to be considered in developing the new generation of tools (increasingly SEEs are becoming a major concern for the trapped radiation environment as proton effects become important for microelectronics).

4) Continuing evaluation of the predictive value of the tools should be carried out. The tools need to be evaluated not only on how well they predict in situ fluxes but also on how well they perform in predicting in situ system performance (the goal of the tools must ultimately be not only scientific fidelity but engineering value).

5) For the user community (operators and designers), standard “meteorology” procedures may prove useful and should be developed: the real-time status of the radiation environment and predictions/forecasts should be available on-line as is now possible for geomagnetic activity.

6) New radiation data sets should be disseminated as widely possible as soon as they become available—the Internet provides a new and unique resource (e.g., the newest version of the CREME codes).

12. Conclusion

The objective of this guide was to address three aspects of the radiation problem. First, a review of the natural and man-made space radiation environments was provided. Second, the methods used to propagate the external environment through the complex spacecraft structures surrounding the point where the internal radiation environment was required were discussed. Third, examples of the environment inside the spacecraft were presented.

Although the intention was not to treat in detail all aspects of the problem of the radiation environment within a spacecraft, a basis for understanding the process of predicting the internal spacecraft radiation environment has been established by dividing the problem into three parts—external environment, propagation, and internal environment. Finally, the consequences of this environment on spacecraft behavior need to be carefully evaluated in developing new tools for modeling the trapped radiation environment. Based on these conclusions, a set of recommendations has been formulated that can be used to delineate future efforts in this area.

13. References

[1] Condon, E. U., and Odishaw, H., *Handbook of Physics*, 2nd ed., McGraw–Hill, New York, 1967.

[2] Roederer, J. G., "Dynamics of Geomagnetically Trapped Radiation," *Physics and Chemistry in Space*, Vol. 2, Springer–Verlag, New York, 1970, p. 166.

[3] Adams, J. H., Jr., "Cosmic Ray Effects on Microelectronics, Part IV," Naval Research Laboratory, NRL Memorandum Rept. 5901, Washington, DC, 1986.

[4] van Lint, V. A. J., "Radiation Effects Testing Short Course," *IEEE 1986 Nuclear and Space Radiation Effects Conference*, Providence, RI, 1986.

[5] Adams, J. H., Jr., Letaw, J. R., and Smart, D. F., "Cosmic Ray Effects on Microelectronics, Part II: The Geomagnetic Cutoff Effects," Naval Research Laboratory, NRL Memorandum Rept. 4506, Washington, DC, 1983.

[6] Van Allen, J. A., "Geomagnetically Trapped Radiation," *Space Science*, Wiley, New York, 1963.

[7] Daly, E. J., "The Evaluation of Space Radiation Environments for ESA Projects," *ESA Journal*, Vol. 12, 1988, pp. 229–247.

[8] Vampola, A. L., "Effects of the March-June Magnetic Storm Period on Magnetospheric Electrons," *Solar-Terrestrial Predictions-IV, Proceedings of a Workshop at Ottawa, Canada, May 18-22, 1992* (Ottawa, Canada), NOAA/SEL, Boulder, CO, 1993.

[9] Knecht, D. J., and Shuman, B., "The Geomagnetic Field," *Handbook of Geophysics and the Space Environment*, edited A. S. Jursa, National Technical Information Service, Accession No. ADA 167000, Springfield, VA, 1985, Chapter 4.

[10] Olson, W. P., and Pfitzer, K. A., "A Quantitative Model of the Magnetospheric Magnetic Field," *Journal of Geophysical Research*, Vol. 79, 1974, pp. 3739–3748.

[11] Voigt, G. H., "A Three Dimensional, Analytical Magnetospheric Model with Defined Magnetopause," *Zeitschuiftfur Geophysik*, Vol. 38, 1972, pp. 319–346.

[12] Tsyganenko, N. A., "A Model of the Cis-Lunar Magnetospheric Field," *Annales de Geophysique*, Vol. 32, Jan.–March, 1976, pp. 1–12.

[13] Langel, R. A., “IGRF, 1991 Revision,” *Transactions of the American Geophysical Union*, Vol. 73, 1992, p. 182.

[14] Barraclough, D. R., “International Geomagnetic Reference Field: The 4th Generation,” *Physics of the Earth and Planetary Interiors*, Vol. 48, 1987, pp. 279–292.

[15] Vette, J. I., Teague, M. J., Sawyer, D. M., and Chan, K. W., “Modeling the Earth’s Radiation Belts,” *Solar-Terrestrial Prediction Proceedings*, edited by R. F. Donnelly, NOAA, Boulder, CO, 1979.

[16] Sawyer, D. M., and Vette, J. I., “AP-8 Trapped Proton Environment for Solar Maximum and Solar Minimum,” 76-06, NSSDC/WDC-A-R&S, 1976.

[17] Vette, J. I., “The AE-8 Trapped Electron Model Environment,” 91-24, NSSDC/WDC-A-R&S, 1991.

[18] Vampola, A. L., “The Space Particle Environment,” *Materials in Space*, Langley Research Center, NASA, June, 1988.

[19] Smith, R. E., and West, G. S. (eds.), *Space and Planetary Environment Criteria Guidelines for Use in Space Vehicle Development, 1982 Revision*. Vol. 1, NASA, TM-82478, 1983.

[20] Huston, S. L., and Pfitzer, K., “A New Model for the Low Altitude Trapped Proton Environment,” *IEEE Nuclear Science and Radiation Effects Conference*, Newport Beach, CA, July 20–24, 1998.

[21] Vampola, A. L., Lauriente, M., Huston, S., and Pfitzer, K., “Validating the New SEE Low Altitude Proton Model,” *Proceedings of the Conference on High Energy Radiation Backgrounds in Space*, Snowmass, CO, July, 1997.

[22] Hess, W. N., “Collected Papers on the Artificial Radiation Belt from the July 9, 1962, Nuclear Detonation,” *Journal of Geophysical Research*, Vol. 68, 1963, p. 605.

[23] Abel, R., Thorne, R. M., and Vampola, A. L., “Solar Cycle Behavior of Trapped Energetic Electrons in Earth’s Inner Radiation Belt,” *Journal of Geophysical Research*, Vol. 99, 1994, pp. 19,427–19,431.

[24] Chan, K., Teague, M. J., Schofield, N., and Vette, J. I., “Modeling of Electron Time Variations in the Radiation Belts,” *Quantitative Modeling of Magnetospheric Processes,* edited by W. P. Olson, American Geophysical Union, Washington, DC, 1979, p. 121.

[25] Paulikas, G. A., and Blake, J. B., “Effects of the Solar Wind on Magnetospheric Dynamics: Energetic Electrons at the Synchronous Orbit,” *Quantitative Modeling of Magnetospheric Processes,* edited by W. P. Olson, American Geophysical Union, Washington, DC, 1979, pp. 180-202.

[26] Baker, D. N., Belian, R. D., Higbie, P. R., and Hones, E. W., Jr., “The Use of >30 KeV Electron Anisotropies at 6.6 R_e to Predict Magnetospheric Substorms,” *Solar-Terrestrial Predictions Proceedings*, edited by R. F. Donnelly, NOAA, Boulder, CO, 1980.

[27] Lyons, L. R., and Williams, D. J., “The Storm and Poststorm Evolution of Energetic (35-560 keV Radiation Belt Electron Distributions),” *Journal of Geophysical Research*, Vol. 80, 1975, pp. 3985–3994.

[28]Taylor, W. W. L., and Lyons, L. R., “Simultaneous Equatorial Observations of 1 to 30-Hz Waves and Pitch Angle Distributions of Ring Current Ions,” *Journal of Geophysical Research*, Vol. 81, 1976, pp. 6177–6183.

[29]Gussenhoven, M. S., Mullen, E. G., Brautigam, D. H., Holeman, E., Jordan, C., Hanser, F., and Dichter, B., “Preliminary Comparison of Dose Measurements on CRRES to NASA Model Predictions,” *IEEE Transactions on Nuclear Science*, Vol. 38, No. 6, December, 1991, pp. 1655–1662.

[30]Vampola, A. L., “Radiation Effects on Space Systems and Their Modeling,” *Space Systems and Their Interactions with Earth’s Space Environment,* edited by H. B. Garrett and C. P. Pike, AIAA, New York, 1980, p. 339.

[31]Janni, J., and Radke, G., “The Radiation Environment and Its Effects on Spacecraft,” *Quantitative Modeling of Magnetospheric Processes,* edited by W. P. Olson, American Geophysical Union, Washington, DC, 1979, p. 634.

[32]Vampola, A. L., “Low Energy Inner Zone Protons—Revisited,” *Workshop on the Earth’s Trapped Particle Environment, Taos, NM, Aug. 1994*, edited by G. Reeves, AIP CP-383, 1996.

[33]Kerns, K. J., Capt., USAF, and Gussenhoven, M. S., “CRRESRAD Documentation,” Phillips Laboratory, Directorate of Geophysics, PL-TR-92-2201, 1992.

[34]Brautigam, D. H., Gussenhoven, M. S., and Mullen, E. G., “Quasi-Static Model of Outer One Electrons,” *IEEE Transactions on Nuclear Science*, Vol. 30, No. 39:(6), 1992, pp. 1797–1803.

[35]Gussenhoven, M. S., Mullen, E. G., and Brautigam, D. H., “Near-Earth Radiation Model Deficiencies as Seen on CRRES,” *Advances in Space Research*, Vol. 14, No. 10, 1994, pp. 927–941.

[36]Hardy, D. A., Hanser, F., and Sellers, B., “The Space Radiation Dosimeter (AFGL-701-2),” *CRRES/SPACERAD Experiment Descriptions*, edited by M. S. Gussenhoven, E. G. Mullen, and R. C. Sagalyn, AF Geophysics Laboratory, Hanscom AFB, MA, 1985.

[37]Vampola, A. L., “ESA Update of AE-8 Using CRRES Data and a Neural Network,” *Radiation Belts Models and Standards, Geophysical Monograph 97,* edited by J. F. Lemaire, D. Heynderickx, and D. N. Baker, American Geophysical Union, Washington, DC, 1996, pp. 297–303.

[38]Vampola, A. L., “Outer Zone Energetic Electron Environment Update,” *Proceedings of the Conference on High Energy Radiation Backgrounds in Space*, Snowmass, CO, July, 1997.

[39]Blake, J. B., and Friesen, L. M., “A Technique to Determine the Charge State of the Anomalous Low Energy Cosmic Rays,” *15th International Cosmic Ray Conference*, Plovdiv, Bulgaria, Vol. 2, 1977.

[40]Cornwall, J. M., “Radial Diffusion of Ionized Helium and Proton: A Probe for Magnetospheric Dynamics,” *Journal of Geophysical Research*, Vol. 77, 1972, p. 1756.

[41]Spjeldvik, W. N., and Fritz, T. A., “Theory of Charge States of Energetic Oxygen Ions in the Earth’s Radiation Belts,” *Journal of Geophysical Research*, Vol. 83, No. A4, 1978, p. 1583.

[42] Fritz, T. A., and Spjeldvik, W. N., “Simultaneous Quiet Time Observations of Energetic Radiation Belt Protons and Helium Ions: the Equatorial α/p Ratio Near 1 MeV,” *Journal of Geophysical Research*, Vol. 84, 1979, pp. 2608–2618.

[43] Adams, J. H., Jr., Silverberg, R., and Tsao, C. H., “Cosmic Ray Effects on Microelectronics, Part I: The Near-Earth Particle Environment,” Naval Research Laboratory, NRL Memorandum Rept. 4506, Washington DC, 1981.

[44] Grigorov, N. L., Kondratyeva, M. A., Panasyuk, M. I., Tretyakova, C. A., Adams, J. H., Blake, J. B., Schultz, M., Mewaldt, R. A., and Tylka, A. J., “Evidence for Anomalous Cosmic Ray Oxygen Ions in the Inner Magnetosphere,” *Geophysical Research Letters*, Vol. 18, 1991, p. 1959.

[45] Cummings, J. R., Cummings, A. C., Mewaldt, R. A., Selesnick, R. S., Stone, E. C., and von Rosenvinge, T. T., “New Evidence for Geomagnetically Trapped Anomalous Cosmic Rays,” *Geophysical Research Letters*, Vol. 20, No. 18, 1993, pp. 2003–2006.

[46] Group, P. D., “Passage of Particles Through Matter; Review of Particle Properties,” *Physics Letters, B*, Vol. 239, No. III, 1990, pp. 1–38.

[47] Winokur, P. S., “Total-Dose Radiation Effects (from the Perspective of the Experimentalist),” *IEEE Nuclear and Space Radiation Effects Conference Short Course*, Vol. II, edited by F. W. Sexton, IEEE, New Orleans, LA, 1992.

[48] Berger, M. J., and Seltzer, S. M., “Penetration of Electrons and Associated Bremsstrahlung through Aluminum Targets,” SP-169, NASA, Washington, DC, 1968, pp. 285–322.

[49] Janni, J. F., “Proton Range-Energy Tables, 1 keV-10 GeV, Part 1,” *Atomic Data and Nuclear Data Tables*, Vol. 27, Nos. 2/3, Academic, New York, 1982, pp. 150–339.

[50] Janni, J. F., “Proton Range-Energy Tables, 1 keV-10 GeV, Part 2,” *Atomic Data and Nuclear Data Tables*, Vol. 27, Nos. 4/5, Academic, New York, 1982, pp. 341–529.

[51] Curgenven, L., and Duncumb, P., “Report 303,” Tube Investments Research Laboratories, 1971.

[52] Brown, D. B., “Total Dose Effects at Dose Rates Typical of Space,” *NSREC Short Course*, IEEE NSREC, 1990.

[53] Jordon, T. M., “Electron Dose Attenuation Kernels for Slab and Spherical Geometries,” AF Weapons Laboratory, AFWL-TR-81-43, 1981.

[54] Jordon, T. M., “NOVICE: A Radiation Transport/Shielding Code; Users Guide,” Experimental and Mathematical Physics Consultants, 87.01.02.01, 1987.

[55] Fermi, E., *Nuclear Physics*, University of Chicago Press, Chicago, IL, 1950.

[56] Evans, R. D., *The Atomic Nucleus*, McGraw–Hill,1955 [reprinted Kliegler Publishing, 1982].

[57] van Lint, V. A. J., Flanagan, T. M., Leadon, R. E., Naber, J. A., and Rogers, V. C., *Mechanisms of Radiation Effects in Electronic Materials*, Vol. 1, Wiley, New York, 1980.

American Institute of
Aeronautics and Astronautics

1801 Alexander Bell Drive, Suite 500
Reston, VA 20191-4344

ISBN 1-56347-367-4